EXPERIMENTAL INVESTIGATION OF THERMAL BEHAVIOUR OF AIR FOIL BEARINGS

by

RAMESH PANDESHWARA SADASHIVA

Presented to the Faculty of the Graduate School of
The University of Texas at Arlington in Partial Fulfillment
of the requirements
for the degree of

MASTER OF SCIENCE IN MECHANICAL ENGINEERING

THE UNIVERSITY OF TEXAS AT ARLINGTON
December 2010

ACKNOWLEDGEMENTS

I sincerely would like to thank my committee chair, Dr. Daejong Kim for his guidance, and support throughout the course of research. I would also like to thank Dr. Kent Lawrence and Dr. Seiichi Nomura for serving as committee members. I would like to thank my friends and colleagues at Microturbomachinery and Energy Systems Laboratory for their help to manufacture the test bearings and valuable advices. My special thanks also go to Dr. Donghyun Lee for his selfless help during the experimentation phase. My sincere thanks to Kermit and Sam in the department machine shop for their support during the fabrication of the test rig. I would also like to acknowledge the financial support provided to me by the Department of Mechanical and Aerospace, The University of Texas at Arlington.

October 26, 2010

ABSTRACT

EXPERIMENTAL INVESTIGATION OF THERMAL BEHAVIOUR OF AIR FOIL BEARINGS

Ramesh Pandeshwara Sadashiva, MS

The University of Texas at Arlington, 2010

Supervising Professor: Daejong Kim

Micro-turbo machinery demands gas bearings to ensure compactness, lightweight and extreme temperature operation. Gas bearings with large stiffness and damping, and preferably of low cost, will enable successful commercial applications. One of the gas bearing which is used for experimental investigation is the Air foil bearing. Previously developed test rig has been modified and further developed for investigating this bearing at various temperatures and speeds. These gas bearings are self acting hydrodynamic air bearings which have been successfully applied to a variety of turbo machinery applications. This new modified test rig also has the capability to measure bearing torque during start-up, shut-down and high speed operation. Load capacity and general performance characteristics can be measured at various temperatures and speeds. This paper describes the new modified test rig and demonstrates its capabilities at different speeds and temperatures. The present research has two phases. First phase includes design modifications and fabrication of the previously developed test rig. Second phase includes experimental investigation of thermal behavior of the air foil bearing. The bearing performance data from this test rig can be used to develop advanced turbo machinery incorporating high temperature oil-free air bearing technology.

A number of tests were accomplished to find the internal temperature profile of air foil bearing at room temperature under various speeds and loads. The temperature profile was collected by instrumenting the gas bearing with multiple thermocouples in order to measure the local temperatures and evaluate thermal gradients in both the axial and circumferential direction. The tests were accomplished with and without cooling air supply. The tests with cooling air supply showed reduction in the temperature values. The cooling method introduced was an axial cooling technique wherein the cooling air is made to flow through the channels made by bump and top foil. Lateral vibration analysis of the shaft was carried out to compute critical speeds, mode shapes and undamped critical speed maps.

TABLE OF CONTENTS

APPENDIX

LIST OF ILLUSTRATIONS

LIST OF TABLES

Table Page

CHAPTER 1

INTRODUCTION

Oil lubricated bearings have been extensively used in variety of turbo machineries due to their high load carrying capacities, but are severely challenged by speed and temperature requirements. These oil lubricated bearings have a very complex lubrication circuit to carry away excess heat and contaminants; also they lubricate balls, inner and outer races. Environmental concerns and extreme operating conditions drive the need for oil-free bearings in small to moderate size turbo machineries. As a result the use of gas film bearings allows for less complicated, lighter weight systems with lower emissions and improved efficiencies compared to oil lubricated bearings. A major advantage of oil free bearings is that they can easily operate at temperatures where the oil lubricated bearings cannot operate. The reason being oil gets overheated at high temperatures resulting in thermal degradation of oil. These oil free bearings have been extensively used in variety of applications such as air cycle machines, high precision instruments, auxiliary power units, turbo compressors, micro turbines and fuel cells. The low viscosity of the gas film demands very small clearances to generate acceptable load capacity. One of the challenges of gas film bearings is the intermittent contact during the start up and shut down as a result they experience excessive drag and wear at start-up and shut down resulting in hydrodynamic instability.

1.1 Air foil bearings and its principle of operation

One type of oil-free bearing is the Air foil bearing [AFB] shown in Figure 1.1. AFB’s are compliant, self-acting hydrodynamic fluid film bearings uses air as lubricant which is not degraded by extreme temperatures. The self-acting hydrodynamic bearing comprise of a shaft that rotates in a bearing sleeve. The hydrodynamic fluid film pressure is built up in the small gap between the rotating shaft surface and bearing sleeve surface. The surface velocity of the shaft drags the fluid into the convergent wedge shaped gap thus generating the hydrodynamic pressure. Foil bearings are unique comprised of bump foils and top foils. The smooth sheet metal foil called as top foil acts as bearing surface and is supported by series of corrugated bump foils which acts as springs to give the compliance to the foil bearing. The spring rate is determined by modulus of elasticity of bump foil material and its geometry. These complaint foils allow the foils to deform under load i.e. the generated hydrodynamic pressures, so that the converging wedge formed between the rotor and bearing surface is maintained even as speed and temperature vary. The compliance also accommodates rotor centrifugal growth, thermal growth and misalignments. The larger film thickness than present in rigid air bearings results in lower power loss due to shearing of the gas film. The thicker gas film and compliant surface combine to make air foil bearings less susceptible to damage caused by the dust particles as the foil surface can move to allow the foreign particle to pass. The relative sliding between top foil and bump foil provides the necessary damping during dynamic motions of shaft. However continuous dry frictions between bump foil/top foils and bump foils/bearing sleeve can cause foil wear even under hydrodynamic operation, and can compromise long term reliability.

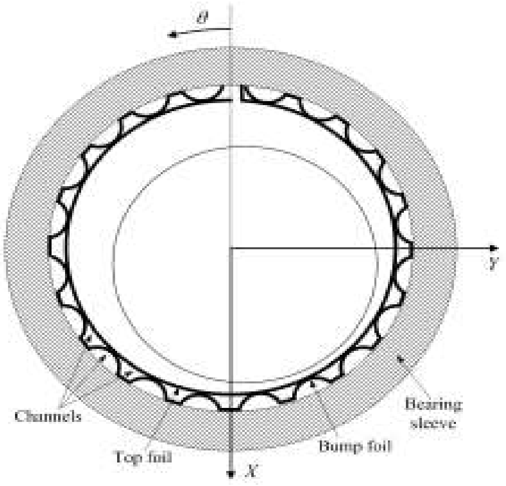

Figure 1.1 Typical air foil bearing

1.2 Areas of concerns of air foil bearings

Air foil bearings are not impervious to thermal environment even though they can operate at very high temperatures and speeds. At high speeds, air film temperature increases significantly due to small heat capacity of air. As the load increases air film becomes thinner and stiffer resulting in bearing's performances depending on elastic properties of bump foils. As the temperature increases, elastic foundation softens resulting in varying bearing's stiffness and damping properties affecting rotor dynamic behavior of the system. Another important concern in AFB's is the spatially variable stiffness which results in varying film thickness and allows the trapping of air. This trapped air undergoes viscous heating leading to formation of localized thermal gradients. These localized thermal gradients lead to distortion of top foil and finally results in failure of AFB's [1].

1.3 Tilting pad bearings and its principle of operation

Another type of oil-free bearing is the tilting pads gas bearing shown in Figure 1.2. The uniqueness of tilting pad gas bearing is the self adjusting pads following the rotor motions and results in low cross-coupled stiffness, thereby eliminating rotordynamic instability. The main drawback is that it has multiple degrees of freedom resulting in complex analytical solutions for estimating force coefficients and the stability characteristics of whole rotor bearing system [2]. Conventional tilting pad bearings may use spherical seat or rocker-type pivots, while flexure pivots are especially suited for gas bearings. However, oil-free environment makes it difficult to adopt conventional ball-socket configuration because of limited reliability of the sliding interfaces. Conventional tilting pad gas bearings cannot accommodate rotor thermal and centrifugal growth, which are very common in high-speed turbo machinery. The drawbacks of conventional tilting pad bearings are overcome by flexure pivot tilting pad bearings (FPTPBs). FPTPBs manufactured by wire-EDM are single piece component (Integral pad bearing configuration) wherein the pads are connected through a flexible web like structure. The rotational stiffness of the pad is very low leading to low cross coupled stiffness, finally eliminating rotor dynamic instability. FPTPBs have notable advantages over the conventional tilting-pad gas bearings such as

(1) FPTPBs have no assembly tolerance stack-up.

(2) Pivot wear due to sliding motion does not exist within the flexure-pivot mechanism.

As a result, the flexure pivot configurations are popular both in gas-lubricated bearings and also in oil-lubricated bearings. One of the technical difficulties faced in adopting FPTPBs to oil-free turbo machinery is the large centrifugal growth of the rotor that comes from high speed operation which is necessary to achieve high power density and efficiency. Due to small bearing clearances in the tilting pad bearings, small changes in rotor diameter causes drastic changes in bearing performances. Radial growth of the rotor at high speeds is due to temperature increases of the bearing that can cause thermal runaway similar to foil gas bearings. To accommodate these rotor growths, pads should be compliant in the radial direction to absorb all possible growths. Flexure-pivot tilting pad bearings with radially compliant pads have been developed to address the issue of large rotor growths. The compliance is achieved by a beam structure behind the pads. Figure below shows one of the possible configurations of FPTPBs with radially compliant pads. Both tilting and radial deflection motions of the pads are achieved by simple beam structures created by wire-EDM.

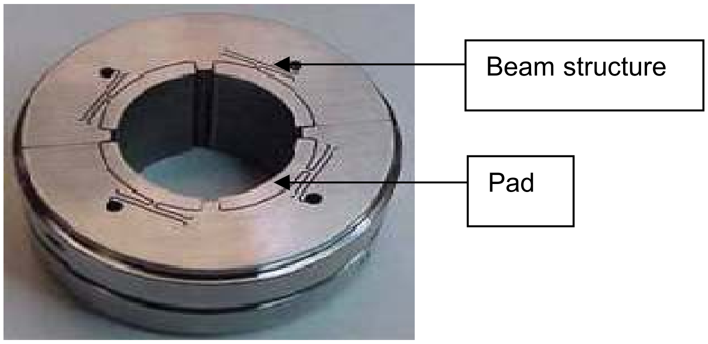

Figure 1.2 FPTPB with radially compliant pads

Another technical difficulty of tilting pad gas bearings is an extension of their applications to flexible rotors. Unlike foil gas bearings, which have shown to effectively accommodate misalignments as well as provide certain levels of coulomb damping to the rotor bearing system, a tight clearance and rather non-conformable bearing surface of the tilting pad gas bearing have limited their applications to well-aligned pseudo-rigid rotors operated below the first bending critical speed. Furthermore, high stiffness of the tilting pad gas bearing and lack of damping mechanism within the bearings (except for the gas film) make the bearings vulnerable to damage upon external shock.

CHAPTER 2

LITERATURE REVIEW

In this section, a number technical papers are listed giving us an insight into the history of gas bearing technology, understanding of gas bearing technology and previous research on the gas bearing technology. Extensive research has been carried out till date on the gas bearing technology. Heshmat et al were the first to work on the gas bearing technology numerically solving the Reynolds equation to obtain the pressure profile, fluid film thickness and load capacity. Then Harman, R. (1981) showed that oil bearings in contrast to air bearings thermally degrade causing the oil to become more acidic and viscous and making it ineffective at performing its multiple functions. Recent advancements in gas bearing design by Heshmat and solid lubricant coating technology by DellaCorte however have provided a revival of research toward applying oil-free bas bearing technology to more demanding applications.

DellaCorte [3] measured the performance of foil bearings at various temperatures and speeds by developing a high temperature (700 °C) and high speed (70000 rpm) test rig and found that maximum load capacity of the bearing reduces as the temperature is increased from 23 to 538 ˚C. Howard, et al experimentally measured the stiffness and damping properties of a foil bearing over a range of sommerfeld number and showed that stiffness was reduced by a factor of 2 from 25 to 538 ˚C and the damping mechanism transformed from viscous to more frictional. They came to a conclusion that decreased material elastic properties resulted in the reduction of bearing performance at elevated temperatures.

Salehi et al [4] explained the thermal characteristics of complaint surface foil bearings analytically and experimentally. They used a Couette approximation to the energy equation to analytically predict resulting temperatures in a foil air bearing. Based on their work they estimated that 80% of the heat is absorbed via conduction into the journal and bearing and the rest is carried away with the air exiting as side leakage. Increase of cooling air temperature helped in providing the above estimate. Experimentally they showed the transient temperature of foil bearings for different loads and speeds.

Radil et al [5] experimentally concluded that radial clearance influences load capacity directly. According to them, an optimum radial clearance resulted in maximum load capacity. Relative to this optimum value there were 2 operating regimes, bearings operating below this optimum value showed low load capacity coefficients and suffered from thermal runaway and conversely bearing operating above the optimum showed decrease in the maximum load capacity coefficients by 20 % with no thermal management problems.

Dykas investigated Thermal and Rotational Contributions to the catastrophic failure mechanism of a thin-Walled journal operating with foil air bearings. Results from his numerical modeling of the bearing–journal system suggested that axial thermal gradients along with centrifugal growth of the journal played a vital role in the catastrophic failure. The bearing was operating in a 540 ˚C ambient environment, at 60000 rpm which supported a load that was only 16% of its calculated load capacity which was based on the rule-of- thumb equation by DellaCorte and Valco.

DellaCorte and Valco [6] had developed a load capacity rule of thumb. This simple, empirical formula allows to estimate acceptable bearing loads for a given size and speed.

Radil and Zeszotek [1] investigated experimentally temperature profile of a compliant foil air bearing. The results showed that, both rotational speed and radial load are responsible for generation of heat with speed playing a more crucial role in the magnitude of the temperatures. The maximum temperature occurred in the middle of the bearing where the air film is thicker rather than at the edge of the bearing where film thickness is minimum. Thermal gradients were common during testing and were strongest in the axial direction from the middle of the bearing to its edges. The temperature profile also indicated the circumferential thermal gradients were negligible.

Peng and Khonsari [7] presented thermo hydrodynamic analysis on temperature distribution of the air film with varying axial stiffness and compared them with experimental results. The temperature distribution of top foil was evaluated by solving the Reynolds and Energy equation simultaneously. Their analysis took into consideration compliance of bearing surface, temperature-viscosity dependence and compressibility of lubricant. The temperature profiles within a wide range of operation conditions were in agreement with the existing experimental data.

Kim and Park [8] designed and constructed the first HAFB, and the load capacity of the HAFB was measured and compared with the hydrodynamic counterpart. A higher load capacity with much less air consumption was observed for the hybrid case with increased efficiency and cooling. This hybrid arrangement resulted in a very small starting torque which is one of the failure modes. They also presented an analytical model which predicted the top foil deflection and sagging effects under hybrid condition. This analytical model showed a very good agreement with the experimental data. Imbalance responses were also predicted using the above model.

Radil, DellaCorte and Zeszotek [9] introduced 3 different thermal management techniques, out of which axial cooling was one of the best techniques to reduce the bearing internal temperature and control the thermal gradients. The other 2 techniques, direct and indirect method of cooling did provide cooling effect to some extent but were not able to control the temperature gradients.

Kim and San Andrés [10] presented a paper on transportation of thermal energy in a high temperature rotor - foil gas bearings system with inner and outer cooling flow. They showed that the outer cooling flow was more effective in eliminating the heat and controlling the bearing internal temperature.

Lee and Kim [11] developed a new thermohydrodynamic model for bump air foil bearings with detailed thermal model of bump foil structures and rotor, which predicts the temperatures of rotor, top foil, bump foil bearing sleeve and air film. This model included the thermal growth of rotor, foil structure and bearing sleeve and rotor centrifugal growth. Their analysis showed that temperature of the rotor increases as the speed and load increases and bearing clearance decreases. The model was compared with published experimental results and showed reasonably good agreement.

Compared to single pad FBs, three padded FBs with hydrodynamic preload [14, 15] have many attractive features such as higher rotor-bearing stability and lower start up friction compared to the circular single pad bearings. Kim et al [13] present simulated thermal behavior of radial FBs with single top foil and preloaded three-pad top foils. They predict lower bulk film temperature of three-padded FBs compared to the one with single top foil under moderate load. The improved thermal behavior of the three-padded FBs was attributed to shorter flow passage length along the circumferential direction.

Sim and Kim [12] developed a computational model to solve the rotor and bearing pad temperatures as well as film temperature simultaneously upon giving adequate boundary conditions. The model solves the Reynolds equation, energy equation and heat flux equation simultaneously through an iterative process considering the rotor's thermal and centrifugal growth. The analysis showed that the nominal clearances had a significant impact on the thermohydrodynamic behavior. They also showed that rotor-bearing system if not provided with proper cooling mechanism can result in thermal runaway.

From the previous works, we infer that very little experimental work has been done so far on one of the main technical issues which is the investigation of thermal behavior and proper thermal management. The scope of this paper is to investigate the thermal behavior of air foil bearings with and without axial cooling method.

CHAPTER 3

RESEARCH OBJECTIVE

3.1 Previous work

Former research assistant Manish Kumar under the guidance of Dr. Daejong Kim designed and constructed a high speed test rig capable of running up to 80,000 RPM. The test rig was then used to experimentally investigate Hybrid air foil bearings. Their experimental investigation dealt with the estimation of load capacity and starting torque of hybrid air foil bearing. They showed that load capacity of the bearing increased under hybrid operation and also the frictional drag associated during startups was reduced considerably.

3.2 Present work

The present work includes redesign and modification of the previous test rig for high temperature capability. The refurbishments also include the design and fabrication of a new test rotor. The present work also includes experimental investigation of thermal behavior of air foil bearings at room temperature. The test data will be used to verify a new computational simulation code currently under development in the lab by other researchers. To compare the measured data with computational model, identification of exact thermal boundary condition is necessary. Thermal contact resistance between the bearing sleeve and its housing which encloses the bearing sleeve is one of the key parameters to be measured. Experimental work in this thesis includes experiment design to measure the thermal contact resistance. The data from this test facility can provide valuable input for bearing development and application. The results from this facility may enable future more extensive applications of foil bearing technologies to oil-free turbo-machinery.

CHAPTER 4

DESIGN AND CONSTRUCTION OF HIGH TEMPERATURE TEST RIG

4.1 Requirements from the test rig

Previously developed test rig was designed for room temperature testing. The rig had to be improved to accommodate high temperature furnace to provide test environment at various temperatures. The new test rig would also experimentally investigate the thermal instability of air foil bearings under different speeds and temperatures by measuring bearing friction torque. The test rig should have the capability to gather basic information about the

1. Load capacity at various speeds and temperatures.
2. Bearing torques during start up and shut down.
3. Thermal runaway.

4.1.1 Description of the old test rig

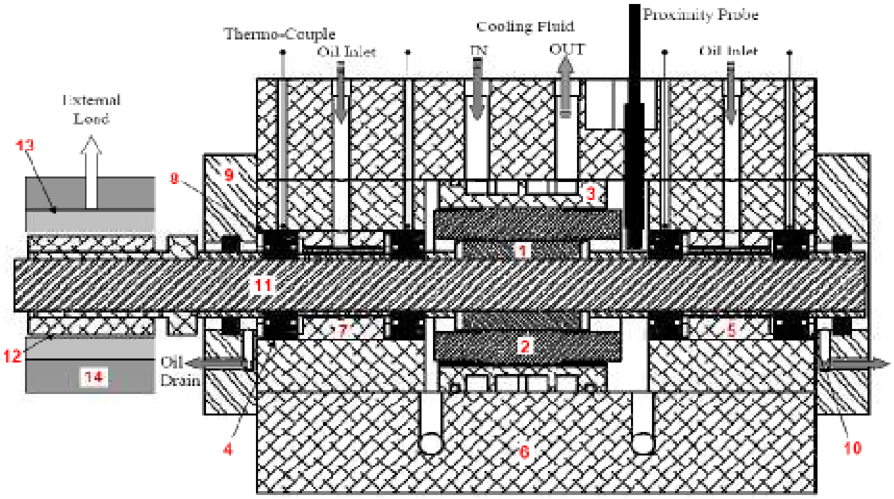

Figure 4.1 Cross-section of old test rig

The electric motor (1) with stator (2) is enclosed by a cooling jacket (3) to dissipate heat. The rotor is supported by four angular contact spindle ball bearings (4) with grease lubrication which in turn are supported by bearing inserts (5). The spindle ball bearings are preloaded using compression type washers (10). Oil jet lubrication set up for the spindle (7) provides the jet lubrication for spindle bearings. Lip seals (8) and end plates (9) to hold the lip seals are also provided. An aluminium housing (6) supports rotor (11), motor and bearing inserts. The overhang shaft is equipped with test section (12) journal to test 1.5” diameter air foil bearing (13) supported by foil bearing housing (14). Due to the short overhang structure, the rig itself is rotordynamically acceptable.

However, the rig has limited capability to test at only room temperature with small bearing. The rig had to be improved to test bigger foil bearings (2” in diameter) at different test environment.

4.2 Redesign of test rig

Redesign of the test rig has gone through two phase efforts. Initial concept was to extend the main shaft, redesign the test section, and put another bearing support at the end of extended shaft. Preliminary run of the rig results in premature failure of the rig and had to redesign the rig again. This chapter details the effort to redesign the test rig.

4.2.1 Description of new test rig (phase 1)

The first phase of redesign is with one solid rotor as shown in the Figure 4.3 below, driven by an electric motor which is capable of rotational speed of about 80,000 rpm. The same electric motor was reused but with longer main shaft. The rotating component (rotor) is colored in brown and red. The main part of the shaft is supported by three angular contact spindle ball bearings with tolerance rings to accommodate rotor vibration more effectively. The spindle ball bearings are preloaded using compression type washers, lubricated by an Alemite 3920 series oil mist lubricator instead of grease lubrication (original rig had grease lubrication). Oil feeders are used to feed oil to the spindle ball bearings from oil mist lubricator through the oil holes in the main aluminum housing. This type of lubricator provides continuous and controlled lubrication to the bearings. End plates hold the aluminium seals and cover the housing on both sides. To provide rugged support to the overhang shaft, another oil-mist lubricated spindle bearing was installed in a split type bearing housing with oil feeder. .

. A custom designed electric furnace as shown in Figure 4.2 was procured. Drawing of the furnace is in Appendix A. The furnace was designed to accommodate torque-rod and three ports for thermo couples, loading mechanism, and fiber optic IR sensor for rotor temperature measurement. The maximum temperature of the test environment by furnace is about 500°C

Figure 4.2 Photo of custom designed electric furnace

The vertical loading of the bearing is accomplished using a wire string with one end attached to the bearing and the other to the loading hanger using a pulley arrangement. A compression type piezo electric load cell (P/N 201B02 SN 26726) is used to measure the bearing torque transmitted via the loading cable. The high temperature measurement of the test insert and the bearing with/without the furnace is carried out using OS550A Series Industrial Infrared (IR) Thermometers. These Thermometers provide non contact temperature measurements up to 4500˚ F.

Preliminary run of the test rig resulted in premature bearing failure below 20,000 rpm. The compression type washers which are used to preload the bearings were not installed properly blocking the oil mist into the ball bearings. As a result ball bearing was damaged due to excess heat. In old rig, grease lubrication did not cause this type of problem. Concentric alignment of the washer was always problematic because the washer OD is slightly smaller than ID of the bearing housing ID.

The premature failure of the bearing lead to identification of several potential problems whenever ball bearing fails during the test. In case of ball bearing damage, disassembly of the ball bearing from the test rig was a cumbersome process. In addition, when test section is worn out and has to be replaced, whole test rig has to be disassembled and re-commissioned. This tedious inefficient operation protocol had to be changed.

4.2.2 Description of new test rig (phase 2)

The second phase of redesigning is based on refurbishing of the Phase I design instead of redesign from scratch. Firstly, the main shaft was cut into two pieces (left section and right section shaft) connected together using a coupling as shown in the Figure 4.4. The left section shaft is press fitted with an extension shaft which is coupled to the right section shaft. The length of the main housing was reduced accordingly and new bearing support housing (at center) was designed and fabricated. The oil feeders were removed, and entry of oil mist into the bearing is direct through the holes on the top of the main housing. The two bearing support housing supports a ball bearing each. This new design allows for the easy disassembly of the ball bearing in case of its damage. The preload spring washers were spot welded to dummy inserts, which in turn free to move along the axial direction with slightly smaller diameter than the ball bearing housing, thus allowing uniform axial preload to the ball bearings. In addition, test section is now isolated from the motor drive, and any change of test journal diameter or coating on it can be done without affecting the main motor drive. The entire test rig is shown in the Figure 4.5.

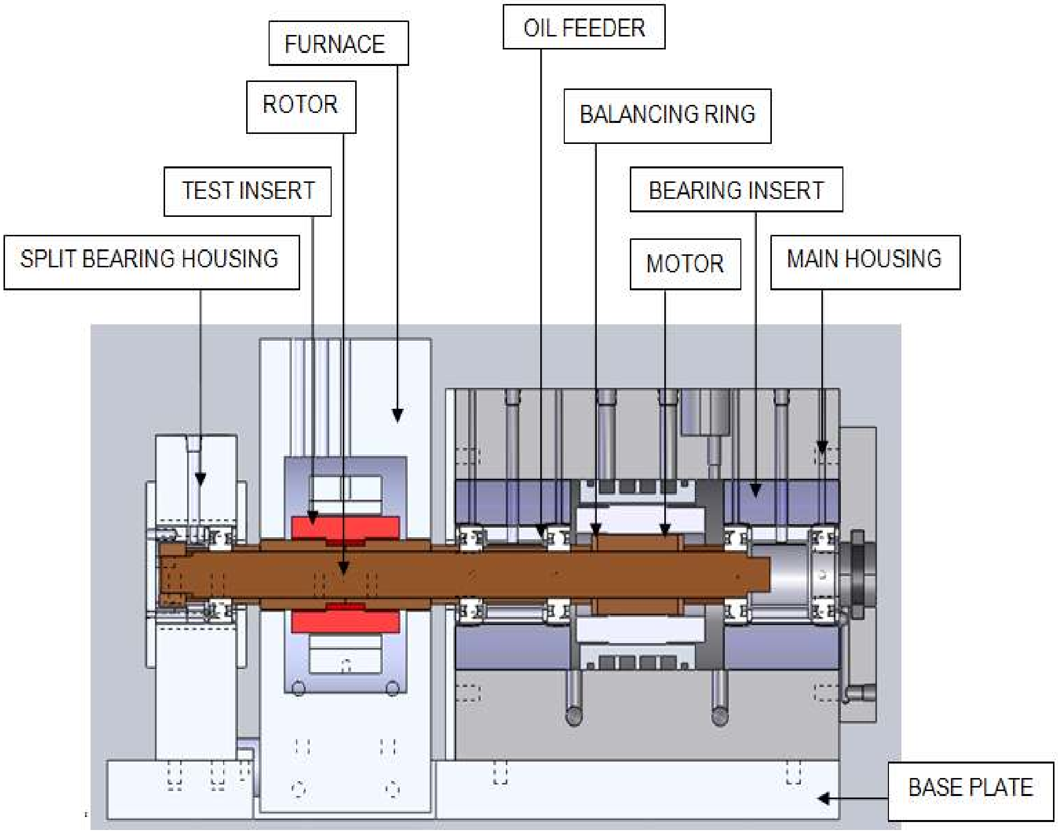

Figure 4.3 General layout of the test rig (First phase)

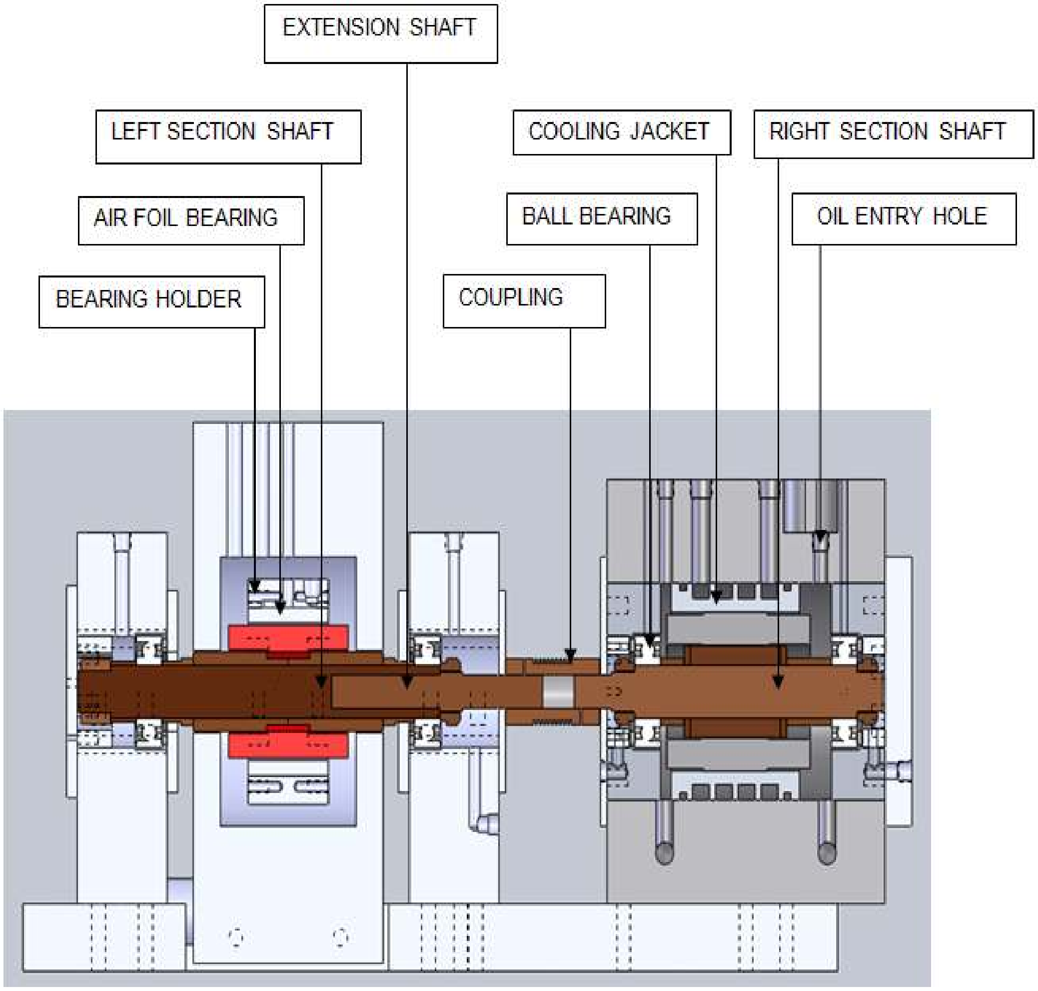

Figure 4.4 General layout of the test rig (Second phase)

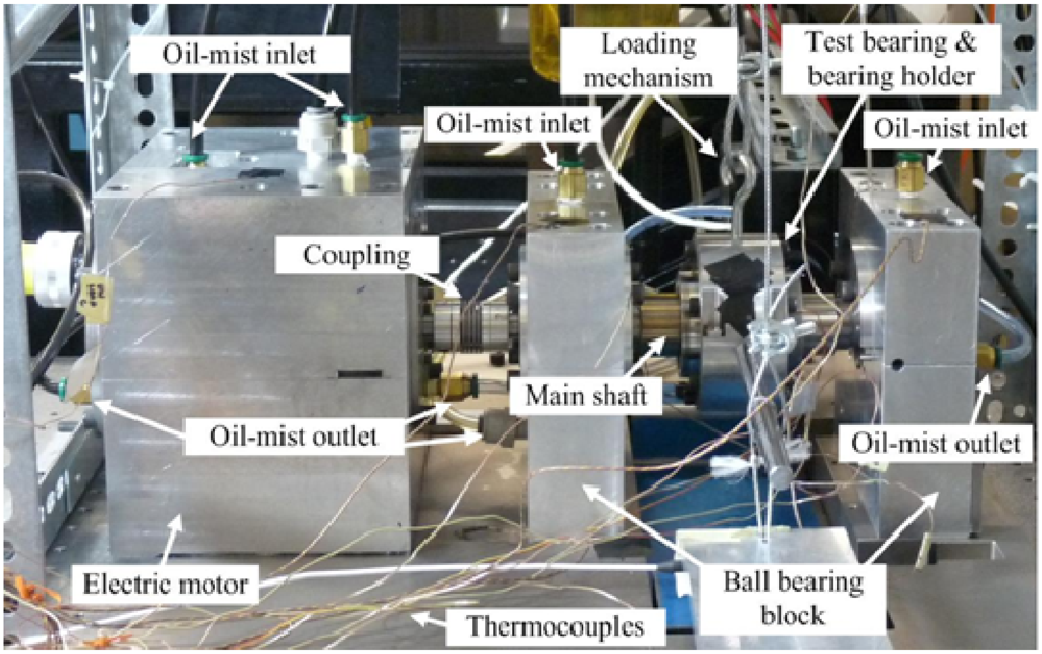

Figure 4.5 Photo of the test rig

Electric motor

The electric motor was procured from Elektromaschinen u. Antriebe AG, Switzerland. The motor is a 2-pole, asynchronous, high-speed and medium frequency motor. The motor has a wound stator and a raw rotor. It can withstand a maximal permissible heating upto 120 K with a coolant (water) temperature of 20° C. Two balance rings were attached to the rotor element on either side of the motor for balancing. The electric motor parameters are given below in the Table 4.1 .

Table 4.1 Electric motor parameters

ELEMENT	PARAMETERS	VALUE
MOTOR	Speed	89,000 rpm
	Frequency	1500 Hz
	Power	2.8 kW
	Peak Power	7 kW
	Voltage	380 V
	Current	6.5 A
STATOR	Insulation Class	F
	Maximum Permissible Heating	120 K
	Coolant Temperature	20 °C
	Coolant	Water
ROTOR	Circumferential Speed	164.9 m/s
	Material of Squirrel Cage	Copper, Ring enforced
	Material of Shaft	Magnetic

4.3 Lubrication system

4.3.1 Alemite 3920 series oil mist lubricator

Alemite oil-mist Lubricator is a centralized lubrication system that continuously and efficiently atomizes oil into small particles and then conveys and delivers the correct amount of the pressurized lubricant to the surfaces requiring lubrication. The Alemite oil mist lubricator allows 0.3 – 1.4 CFM of oil-air mist with 120 VAC power supply.

The components of Oil mist lubricator as shown in Figure 4.6 includes

1. Float switch - Indicates when oil replenishment is required by providing a signal.
2. Filter/Regulator – Filtering the air and improves mist generation performance.
3. Air solenoid Valve - Allows for automatic on or off operation.

4. Mounting plate - Allows quick and easy installation.

The various components of oil reservoir shown in the Figure 4.7 are

1. Relief value - Provides over-pressure protection.
2. Pint nylon reservoir - Allows visual inspection of oil-level & mist generation.
3. Refill loader fitting - Assures contamination-free oil replenishment
4. Aluminium mist head - Provides corrosion protection for long trouble-free service.
5. Oil pick-up screen - Prevents entrance of contaminants into mist generator.

Figure 4.6 Oil mist Lubricator (courtesy- Alemite)

Figure 4.7 Various components of reservoir (courtesy- Alemite)

4.4 Rotordynamic Analysis

Rotordynamic analysis of a new test rig was carried out using the XL ROTOR software which is the commercial software that solves rotor dynamics. Lateral vibration analysis of the shaft was carried out to compute critical speeds, mode shapes and undamped critical speed maps. Analysis was carried out under undamped conditions because the shaft was supported on the rigid ball bearings with little damping and for conservative analysis purpose.

In the analysis, shaft was modeled as series of beam elements whose input table of beam and station definitions are shown in the Table 4.2. Shaft was modeled into 24 stations with bearing at stations 3, 12, 18 and 22 as shown in the Figure 4.8. The flexible coupling connecting the motor and test section is modeled as equivalent beam element with identical lateral stiffness. Lateral stiffness of the coupling was estimated by measuring the damped free vibration. Details are in section 4.4.1. Estimated lateral stiffness of the coupling was 2303.836 N/m. The polar moment of inertia and transverse moment of inertia of the added weight at station 8 were calculated using (1)and (2).

$$I_p = \frac{1}{2} m (r_1^2 + r_2^2) \tag{1}$$

$$I_t = \frac{1}{12} m \left[3(r_2^2 + r_1^2) + h^2 \right] \tag{2}$$

Where m is the mass of the added weight, r_1 and r_2 are the inner and outer radii of the added weight; h is the length of the added weight.

Table 4.2 Shaft input table of beam and station definitions

INPUT TABLE OF BEAM AND STATION DEFINITIONS, MORE THAN ONE BEAM PER STATION IS OK

Station	Length	OD	ID	Density	Elastic Modulus	Shear Modulus	Added Weight	Added Ip	Added It	Speed Factor
#	meters	meters	meters	kg/m^3	N/m^2	N/m^2	kg	kg-m^2	kg-m^2	
1	0.015	0.02579	0	8000	2.00E+11	8.00E+10	0	0	0	1.0
2	0.012	0.02	0	8000	2.00E+11	8.00E+10	0	0	0	1.0
3	0.012	0.02	0	8000	2.00E+11	8.00E+10	0	0	0	1.0
4	0.009	0.02	0	8000	2.00E+11	8.00E+10	0	0	0	1.0
5	0.0056	0.02	0	8000	2.00E+11	8.00E+10	0	0	0	1.0
6	0.03445	0.03	0	8000	2.00E+11	8.00E+10	0	0	0	1.0
7	0.01	0.05	0	8000	2.00E+11	8.00E+10	0	0	0	1.0
8	0.01	0.05	0	8000	2.00E+11	8.00E+10	0.35	5.95E-04	3.06E-04	1.0
9	0.03445	0.03	0	8000	2.00E+11	8.00E+10	0	0	0	1.0
10	0.0056	0.02	0	8000	2.00E+11	8.00E+10	0	0	0	1.0
11	0.009	0.02	0	8000	2.00E+11	8.00E+10	0	0	0	1.0
12	0.012	0.02	0	8000	2.00E+11	8.00E+10	0	0	0	1.0
13	0.0106	0.0254	0	8000	2.00E+11	8.00E+10	0	0	0	1.0
14	0.0374	0.0127	0	8000	2.00E+11	8.00E+10	0	0	0	1.0
15	0.02166	1.00E-03	0	8000	2.00E+11	8.00E+10	0	0	0	1.0
16	0.01734	0.0127	0	8000	2.00E+11	8.00E+10	0	0	0	1.0
17	0.0106	0.0254	0	8000	2.00E+11	8.00E+10	0	0	0	1.0
18	0.012	0.02	0	8000	2.00E+11	8.00E+10	0	0	0	1.0
19	0.011	0.02	0	8000	2.00E+11	8.00E+10	0	0	0	1.0
20	0.048	0.0345	0	8000	2.00E+11	8.00E+10	0	0	0	1.0
21	0.021	0.02	0	8000	2.00E+11	8.00E+10	0	0	0	1.0
22	0.012	0.02	0	8000	2.00E+11	8.00E+10	0	0	0	1.0
23	0.012	0.01488	0	8000	2.00E+11	8.00E+10	0	0	0	1.0
24										1.0
2	0.012	0.023	0.02	2700	6.90E+10	2.60E+10				1.0
4	0.009	0.023	0.02	2700	6.90E+10	2.60E+10				1.0
5	0.0056	0.0254	0.02	2700	6.90E+10	2.60E+10				1.0
10	0.0056	0.0254	0.02	2700	6.90E+10	2.60E+10				1.0
11	0.009	0.023	0.02	2700	6.90E+10	2.60E+10				1.0
19	0.011	0.0254	0.02	2700	6.90E+10	2.60E+10				1.0
21	0.021	0.0254	0.02	2700	6.90E+10	2.60E+10				1.0

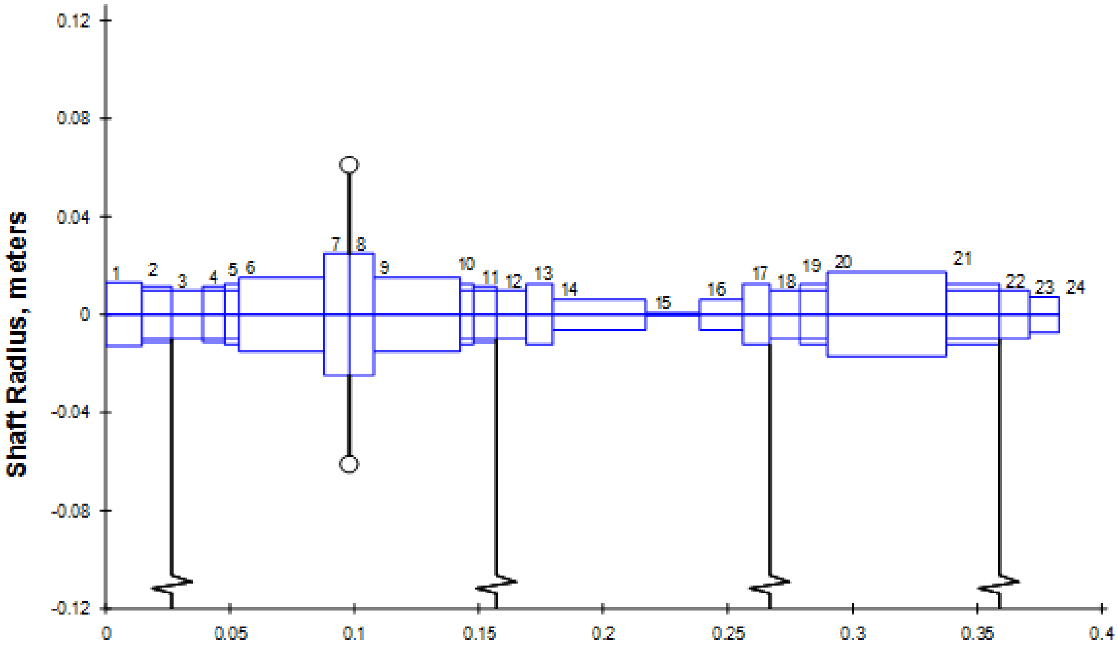

Figure 4.8 Rotor model with 24 stations

The undamped critical speed map of the rotor is shown in the Figure 4.9. The map shows the variation of critical speed with the bearing support stiffness. The undamped critical speed analysis provides an appropriate indication of where critical speeds will occur for the rotor-bearing system. These determinations of critical speeds are important because at these speeds response to imbalance is maximum. Since the shaft has a rigid support from the ball bearings, and therefore considering the higher bearing stiffness value of 1e6 (estimated from internal module within XLRotor) in the critical speed map the first four natural frequencies related to rigid body modes of motor section and test section are 11483.8 cpm, 17561.4 cpm, 20987.7 cpm and 27144.1 cpm. From the critical speed map it can be seen that the critical speeds for the first 4 modes occur below 30000 rpm. The fifth critical speed is related to bending mode of test section rotor, and it appears at above 100,000 rpm which is far above the maximum operating speed limit of the motor. Between the fourth and fifth modes there is a wide operating range without any critical speeds which typical operating speed of the test rig falls within. Most rotor-bearing systems operate between the extremes of low and high bearing stiffness and below the first bending mode.

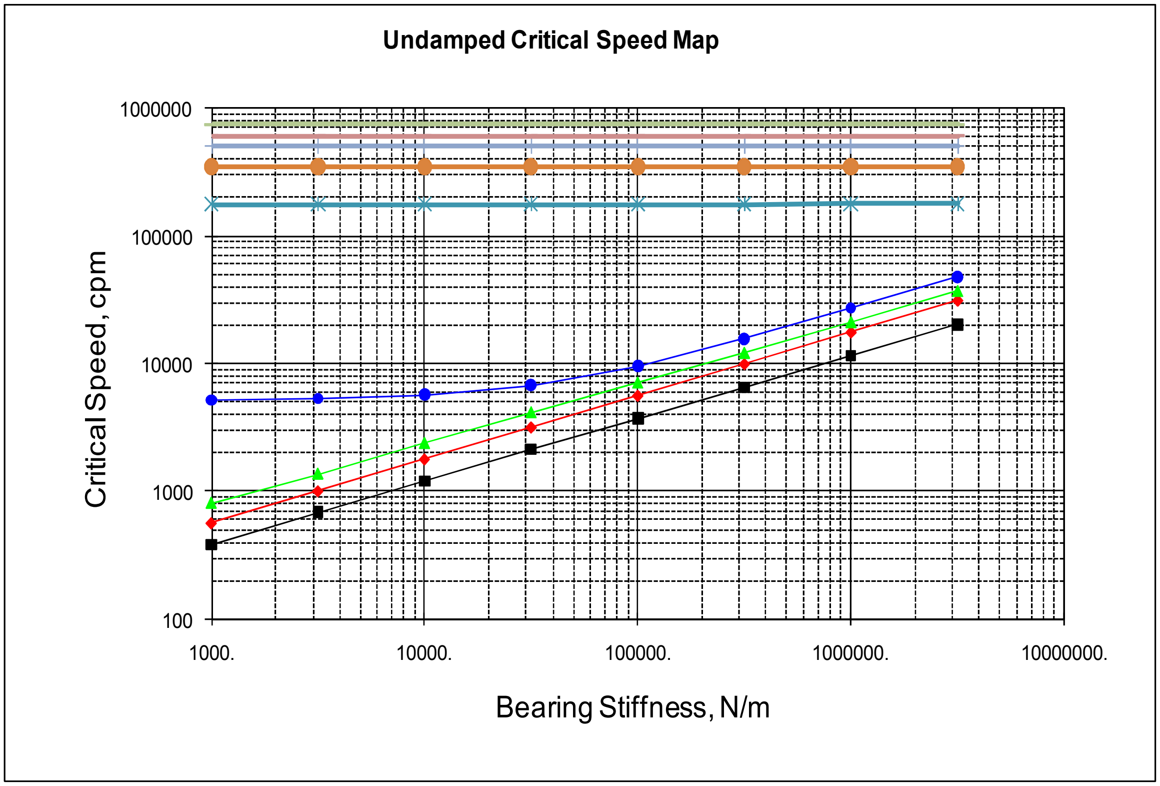

Figure 4.9 Critical speed map of the rotor

Various modes shapes have been shown below. Figure 4.10 shows the first cylindrical mode shape plot. It can be observed that the first cylindrical mode shape is cylindrical mode of the test section. From Figure 4.11, second cylindrical mode shape plot at the motor section can be observed. Figure 4.12 shows the third mode shape plot which is the conical mode at the test section. Figure 4.13 Fourth mode shape plot: conical mode of motor section (a) 2-D plot (b) 3-D plot

shows fourth mode shape plot which is the conical mode observed at the motor section. The fifth mode which is the first bending mode of the test section can be observed in Figure 4.14.

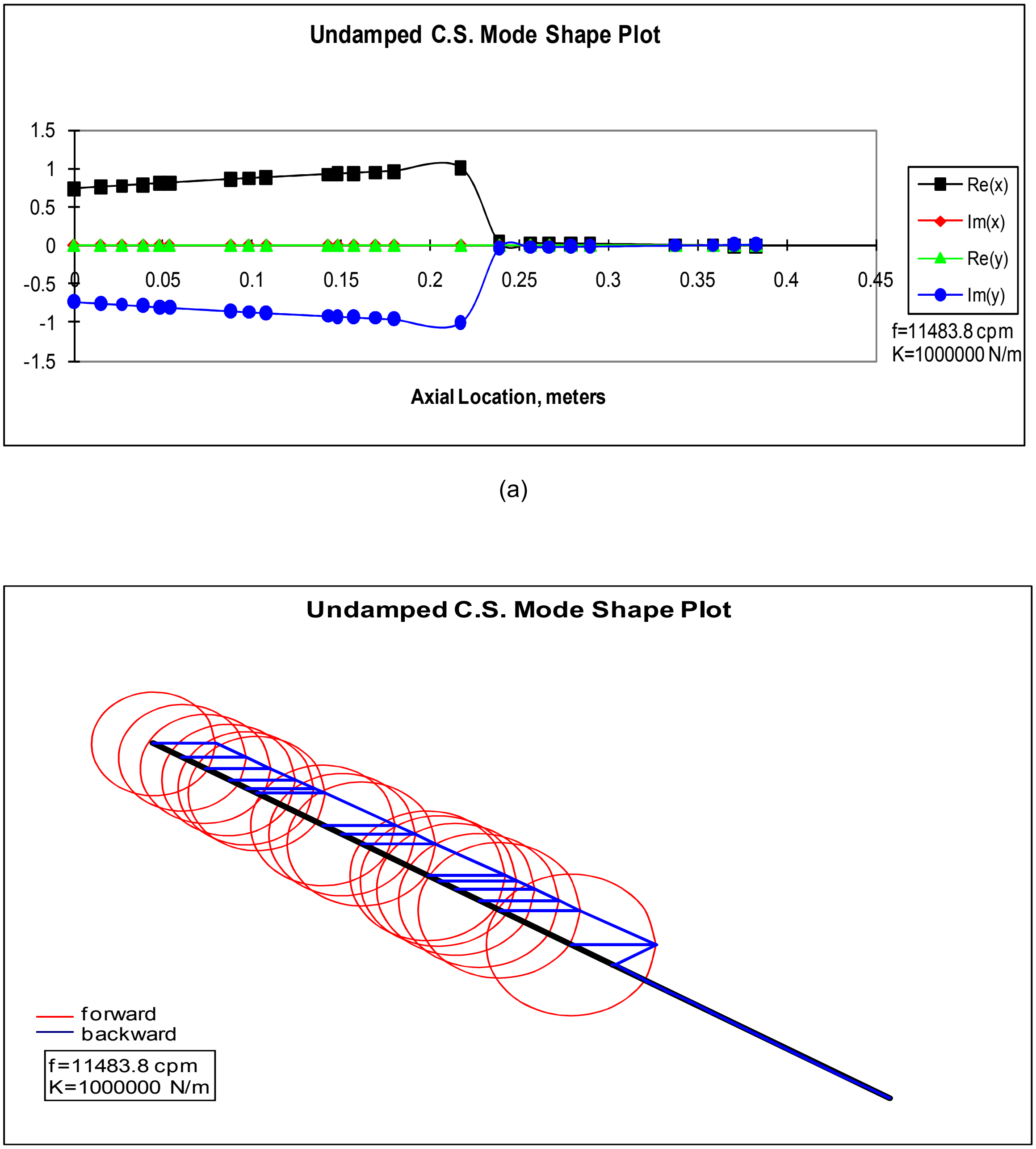

(a)

(b)

Figure 4.10 First mode shape plot: cylindrical mode of test section (a) 2-D plot (b) 3-D plot

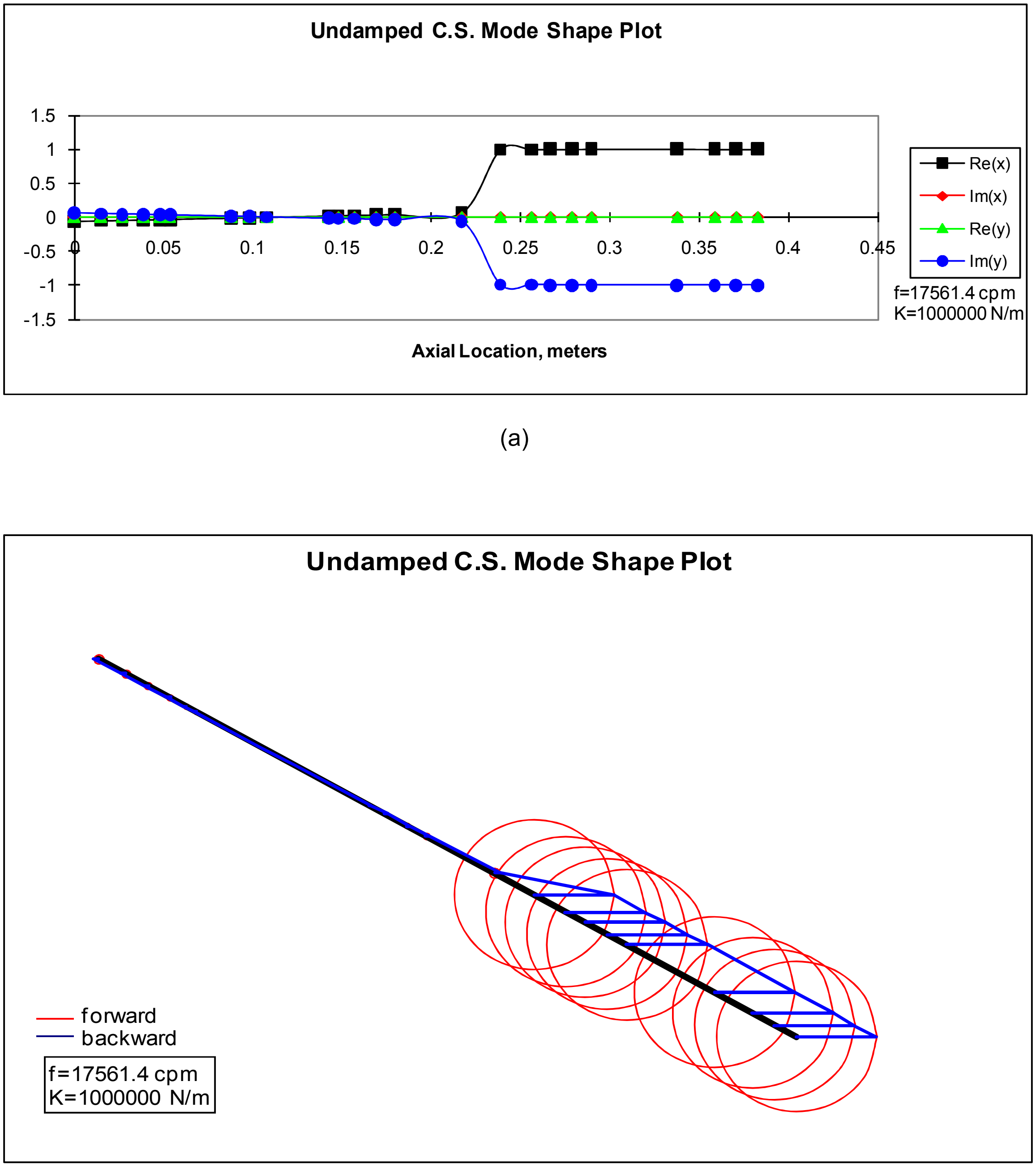

(a)

(b)

Figure 4.11 Second mode shape plot: cylindrical mode of motor section (a) 2-D plot (b) 3-D plot

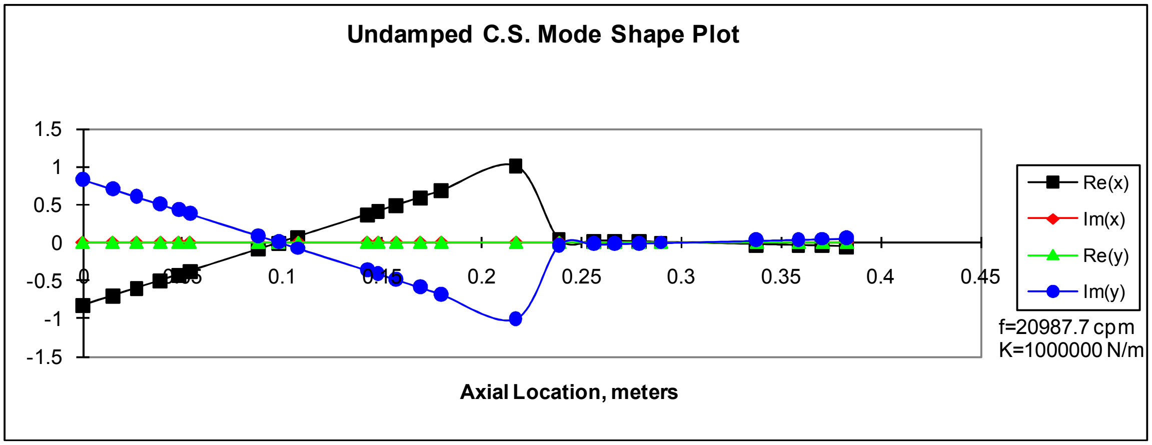

(a)

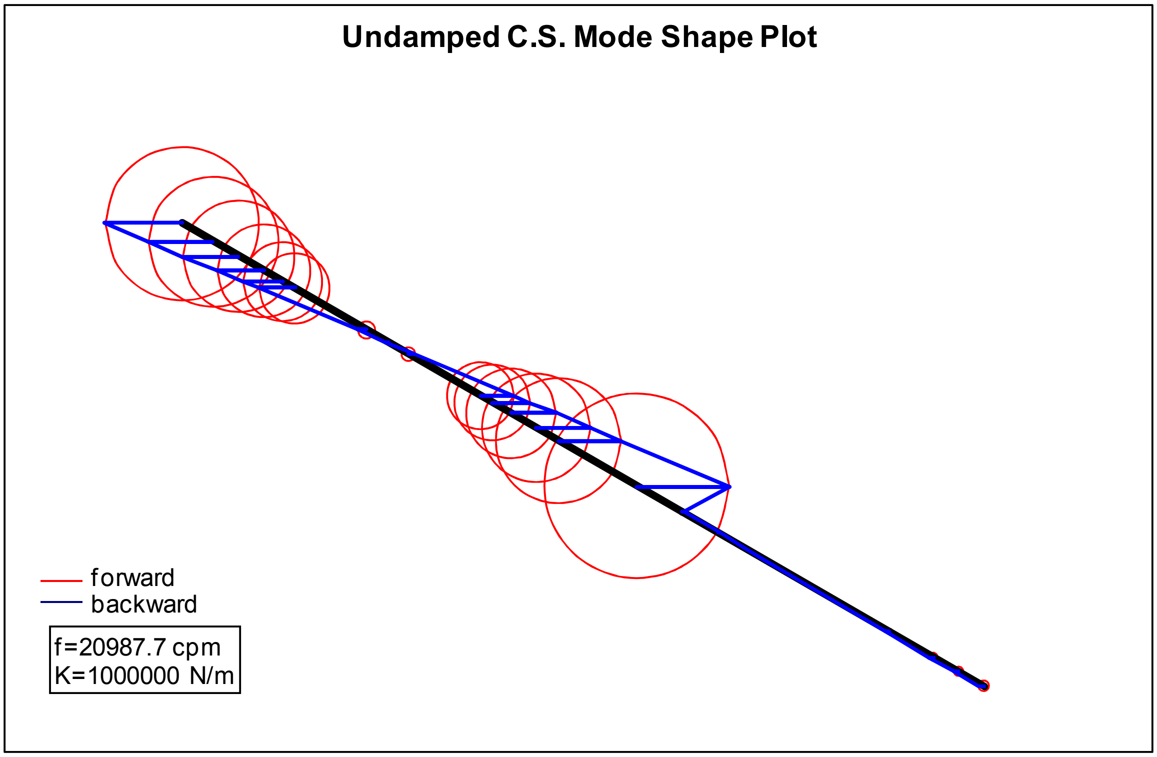

(b)

Figure 4.12 Third mode shape plot: conical mode of test section (a) 2-D plot (b) 3-D plot

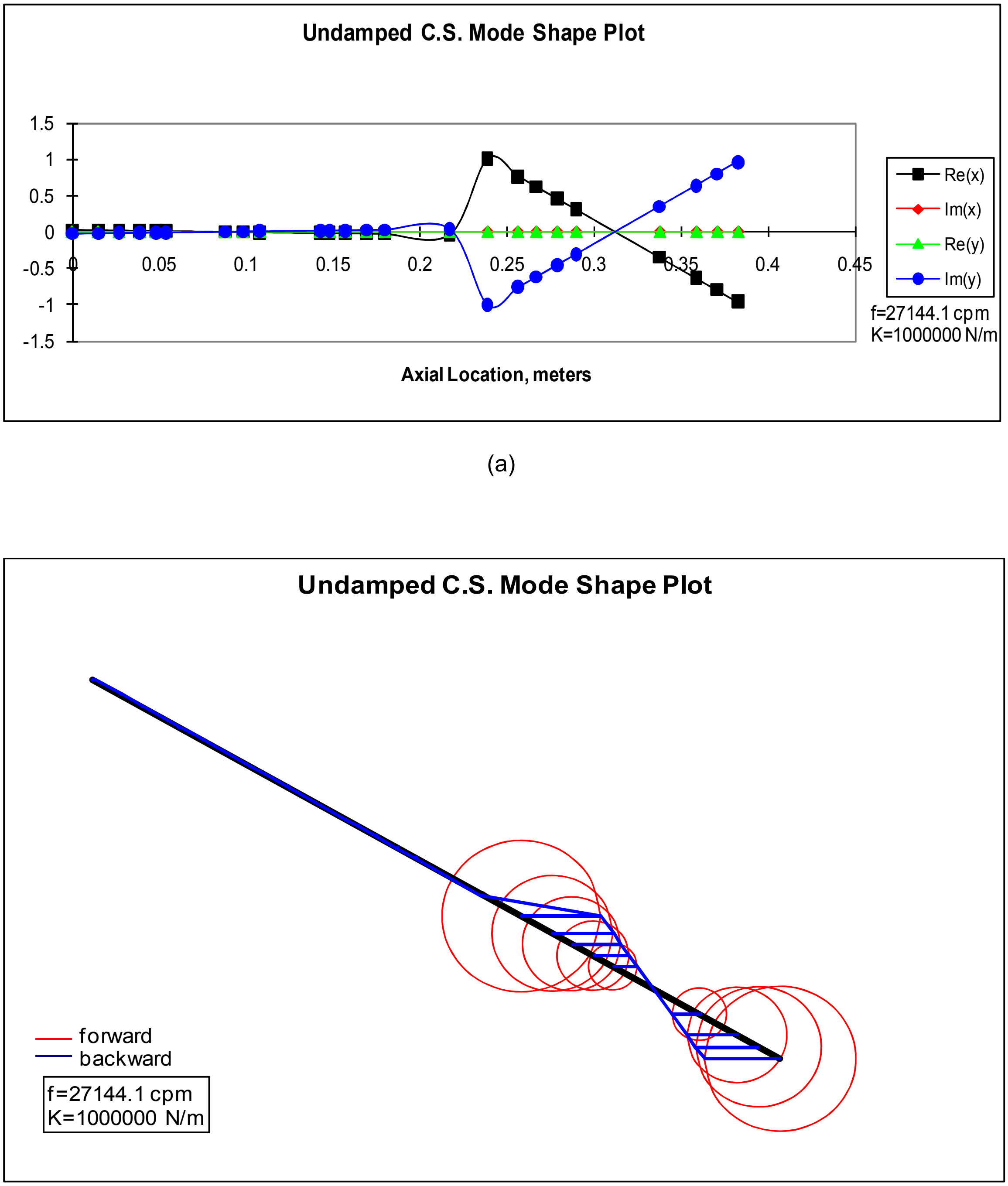

(a)

(b)

Figure 4.13 Fourth mode shape plot: conical mode of motor section (a) 2-D plot (b) 3-D plot

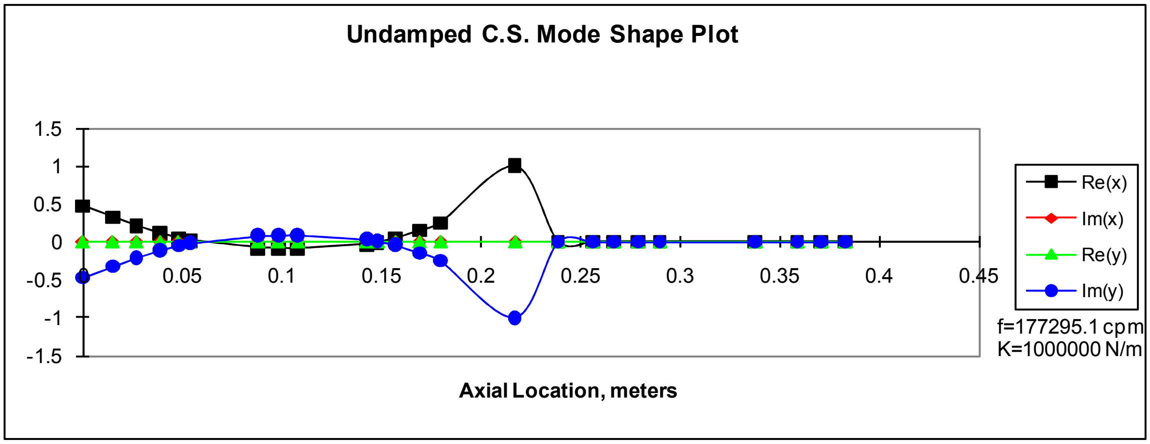

(a)

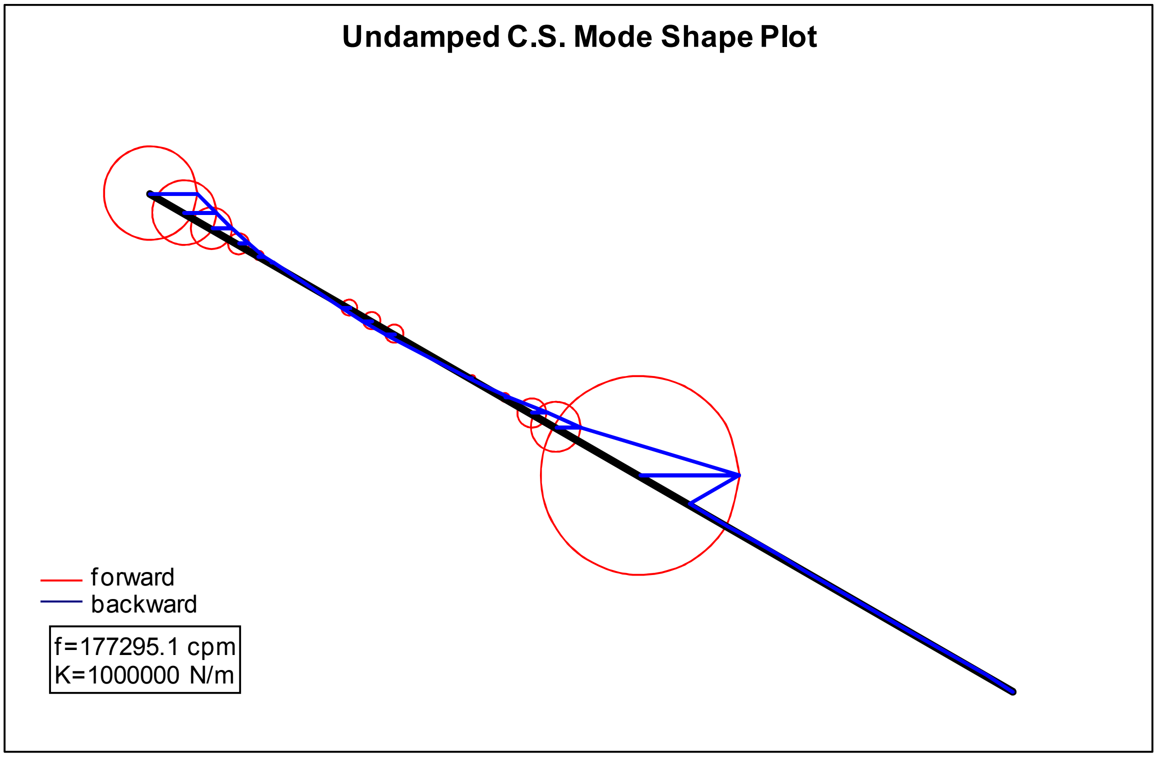

(b)

Figure 4.14 Fifth mode shape plot: first bending mode of test section (a) 2-D plot (b) 3-D plot

4.4.1 Estimation of coupling's lateral stiffness

An impulse load is applied to the coupling to excite the coupling instrumented with accelerometer. From the accelerometer signals, time period and logarithmic decrement is obtained which can be used to get the stiffness value. From this stiffness value, diameter of the beam element is calculated using the beam theory equation.

From the sine curve obtained from the accelerometer we calculate the successive peaks of amplitude (X1 and X2) and time period (T). From the Amplitudes X1 and X2, we calculate the logarithmic decrement (δ) using(3),

$$\delta = \ln\left(\frac{X1}{X2}\right) \tag{3}$$

From logarithmic decrement, we calculate the damping (ζ) using(4),

$$\delta = \frac{2\pi\zeta}{\sqrt{1-\zeta^2}} \tag{4}$$

Using the time period (T) obtained from the curve we get the damped natural frequency (ω_d) and undamped natural frequency (ω_n) using (5) and (6)

$$\omega_d = \frac{2\pi}{T} \tag{5}$$

$$\omega_n = \frac{\omega_d}{\sqrt{1-\zeta^2}} \tag{6}$$

From the undamped natural frequency we get the lateral stiffness (K) of the coupling from ω_n and mass of the coupling (M) using(7)

$$\omega_n = \sqrt{\frac{K}{M}} \tag{7}$$

From the above lateral stiffness, equivalent diameter of the beam element (d) was calculated using

$$K = \frac{48EI}{L^3} \tag{8}$$

Where E is modulus of elasticity, L is the length of the beam element and I is the polar moment of inertia given by

$$I = \frac{\pi d^4}{64} \tag{9}$$

CHAPTER 5

AIR FOIL BEARING FOR TEST AND INSTRUMENTATION

5.1 Description of test air foil bearing

Figure 5.1 describes the concept of hydrodynamically preloaded three-pad air foil bearing. It consists of a 3 top foils, 6 bump foils and a bearing sleeve. C is the nominal radial clearance between the rotor and a virtual bearing formed by pad circle, and C_{SB} is the actual minimal clearance of entire bearing. Preload is the dimensional difference between bearing center and pad circle center. Non-dimensional preload r_p is defined as $r_p=1-C_{SB}/C$. Figure 5.2 shows the photo of actual three pad bearing used for experimentation. Figure 5.3 shows the complete bearing assembly with bearing holder and end plates.

The bearing sleeve is made of age-hardened Inconel 718 and is provided with axial slots throughout the length. The trailing edge of the top foil and one end of the bump foil are inserted into these axial slots. These axial slots are fabricated using electro discharge machining process to obtain the required high precision. The bearing sleeve is supported by split stainless steel 316 housing. End plates are provided to avoid the top foil and bump foil coming out of the axial slots. Top foils are instrumented with two thermocouples, one at the center and other at the edge (18mm from the center towards the cooling air plenum chamber) to investigate the thermal behavior. The top foil made of stainless steel is formed using a forming jig as shown in the Figure 5.6. After it is formed, they are subjected to heat treatment process by keeping it in the furnace. The bump foil made of stainless steel 316 is formed using a forming jig shown in the Figure 5.7. The intricate design of forming jig is fabricated using the electro discharge machining process. The bump foil is also subjected to heat treatment. Generally compared to single pad foil bearings, three padded foil bearings with hydrodynamic preload have many attractive features such as higher rotor-bearing stability and lower start up friction compared to the circular single pad bearings. The air foil bearing parameters are listed in the Table 5.1.

Table 5.1 Air foil bearing parameters (unit: mm)

Rotor radius	25.035
Bearing length	37.5
Bearing radius	25.106
Top foil thickness	0.152
Bump foil thickness	0.127
Bump height	0.49
Nominal clearance	0.071

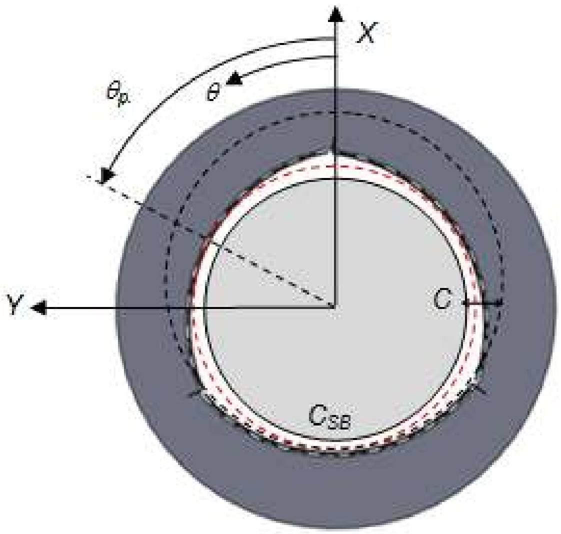

Figure 5.1 Description of three pad configuration with and coordinate system

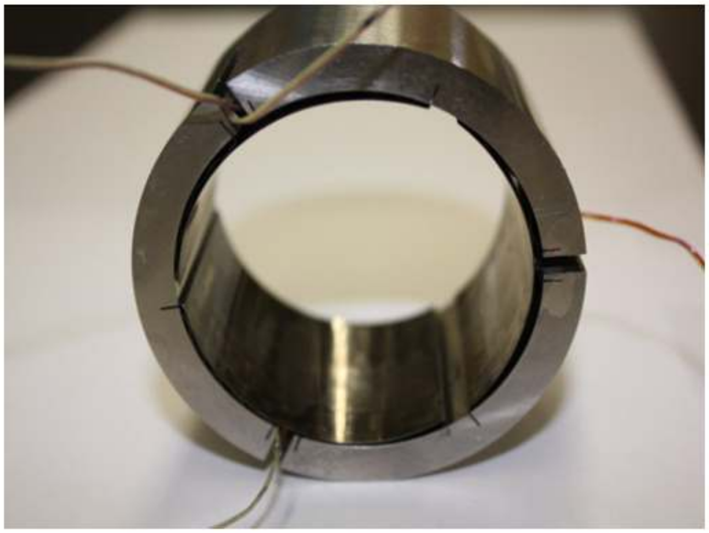

Figure 5.2 Photo of the three pad bearing

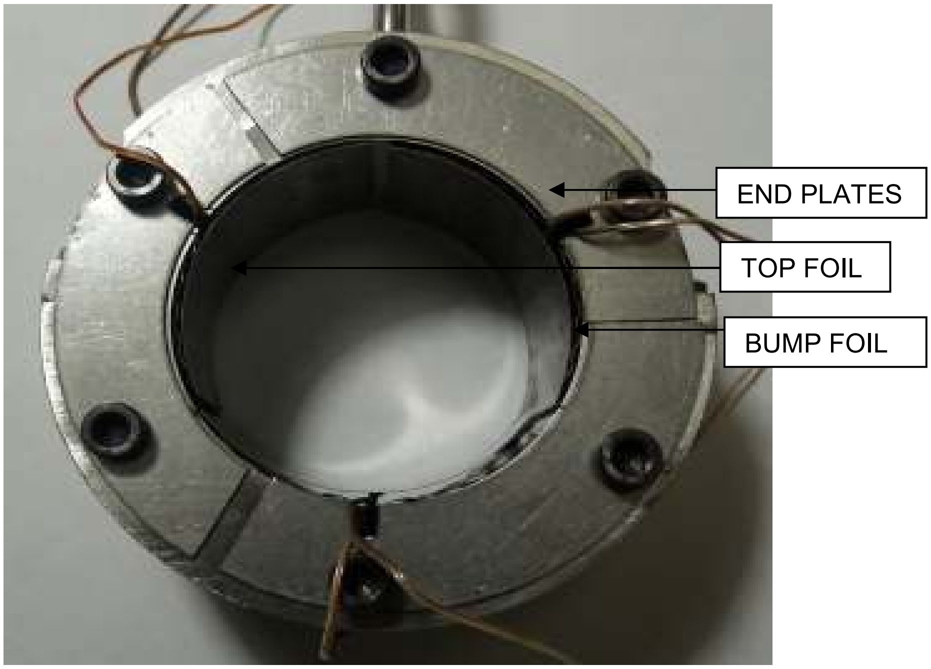

Figure 5.3 Assembled test air foil bearing

Figure 5.4 Photo of top foil with two thermocouples

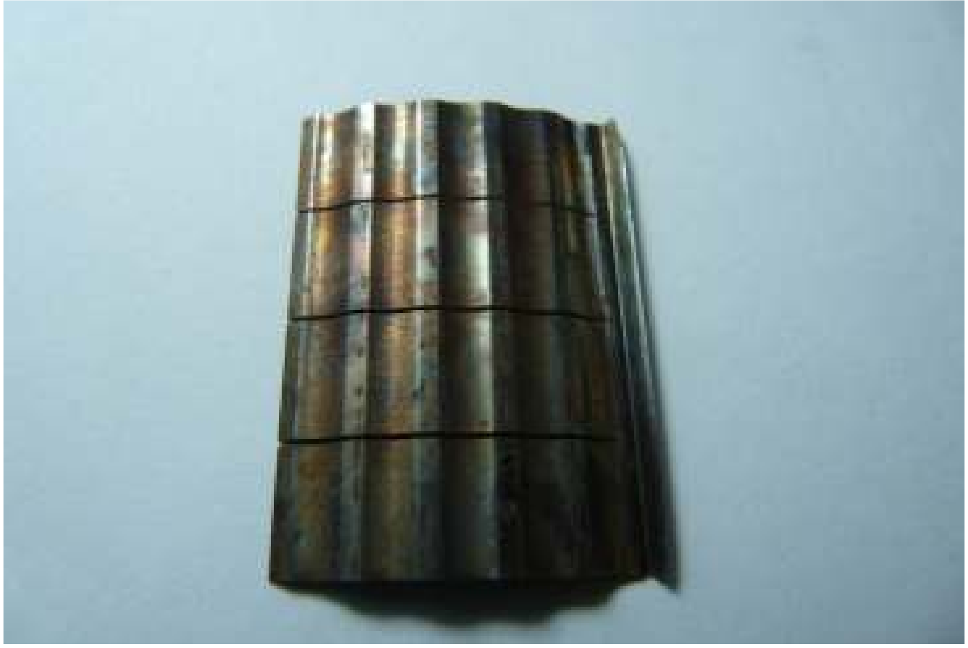

Figure 5.5 Photo of bump foil

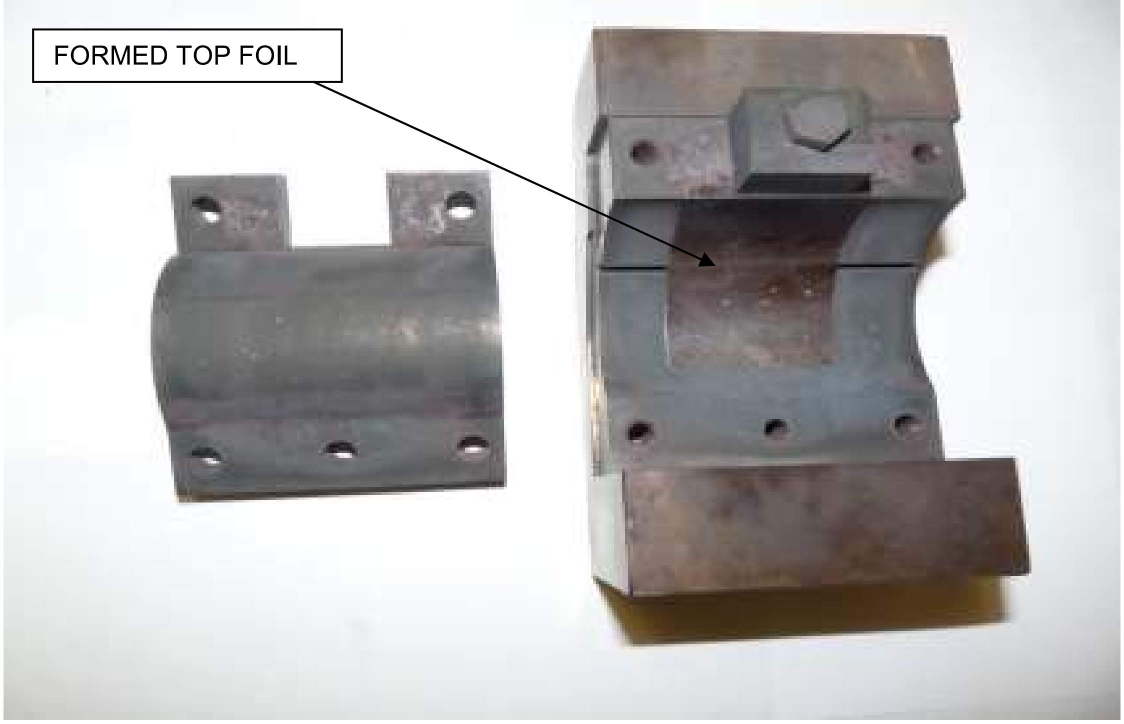

Figure 5.6 Top foil forming jig

Figure 5.7 Bump foil forming jig

5.2 Test bearing instrumentation

Thermocouples were attached on the top foil to measure the thermal behavior. Insulated K-type thermocouple (P/N 5TC-TT-K-30-36) was used. Attaching the uninsulated thermocouples directly on the top foil was not a good method because of its ability to pick up the electrical noise signals which resulted in too many fluctuations of temperature values. This problem was overcome by applying very thin super glue coating on the top foil and then attaching the thermocouple using the high temperature epoxy. This layer of super glue provides the required electrical insulation and results in better measurement of temperature. Two thermocouples were attached on each of the loaded and unloaded top foil at the center and edge as shown in Figure 5.8. The temperature data was recorded using a USB data acquisition system (P/N OMB DAQ 3000). The scan rate and sampling frequency were 5 and 15 scans/second respectively. The bearing frictional torque was measured using a piezoelectric compression type load cell (P/N 201B02 SN 26726) as shown in the Figure 5.9.

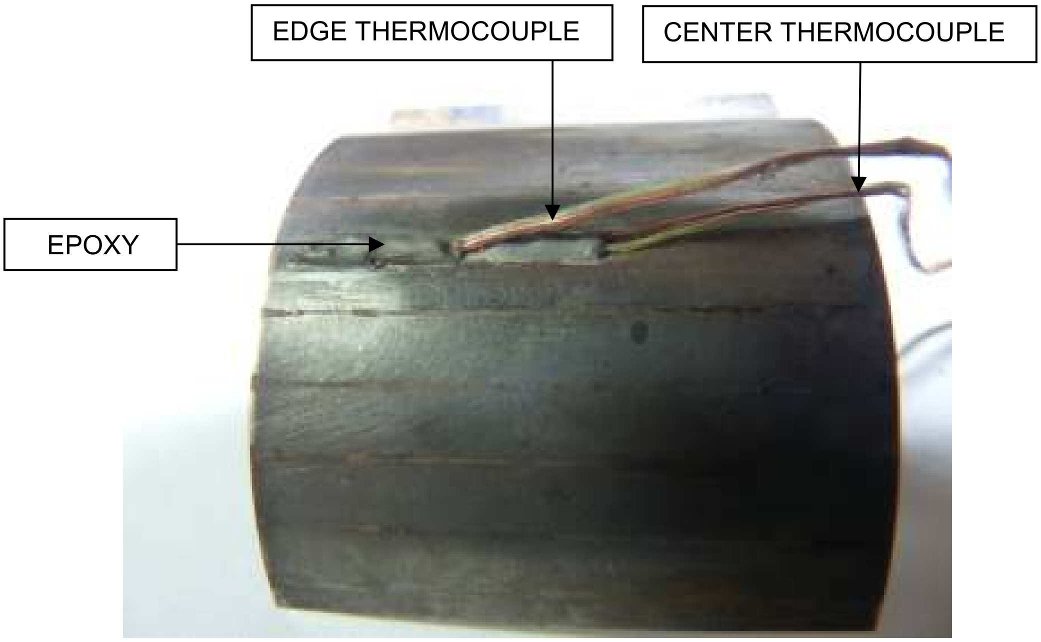

Figure 5.8 Top foil with thermocouple attached

Figure 5.9 Compression type piezoelectric load cell

5.3 Cooling chamber design

Cooling air was required to bring down the temperature of the foil structure. Axial cooling method is used wherein cooling air is supplied through the channels formed by bump foil and top foil as shown in the Figure 5.10.

To provide axial cooling air to the bearing, one side of the bearing is attached with a cooling jacket as shown in the Figure 5.12. Cooling air is supplied to the annular chamber of the cooling jacket first and then chamber distributes the cooling air to all the channels formed by bump foil and top foil. The chamber temperature is measured using the thermocouple attached to the cooling jacket as shown in the Figure 5.11. The thermocouple was inserted inside a small diameter tubes, whose one end was attached to the cooling jacket and the other end to a small rectangular (1in X 1in) aluminum block through 4-40 screws. Figure 5.12 shows a description of the test section with cooling jacket and thermocouples attached. One side of the test journal is exposed to ambient air while the other side is exposed to the cooling air chamber. Figure 5.13

shows the cross section of the test rig showing the cooling air path (Blue arrows) and heat transfer mechanisms (Red arrows).

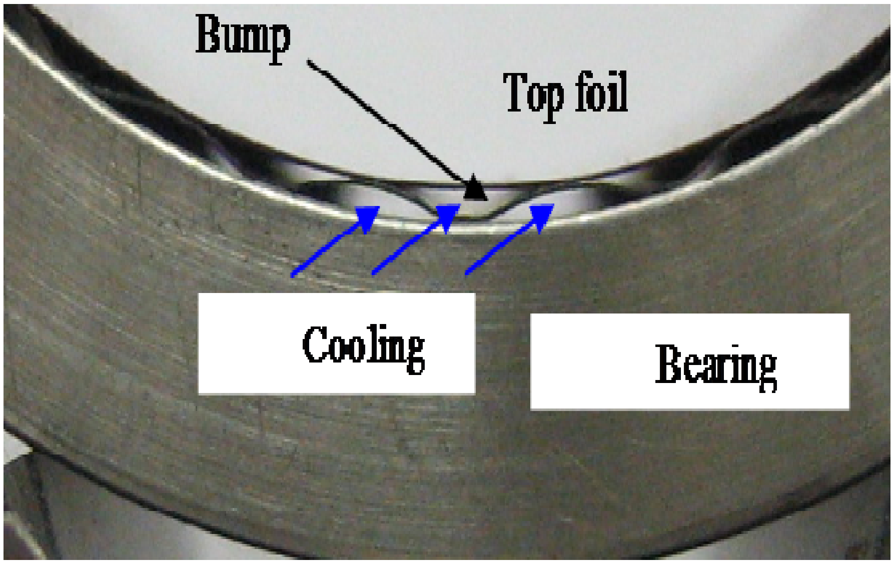

Figure 5.10 Photo showing the axial cooling method

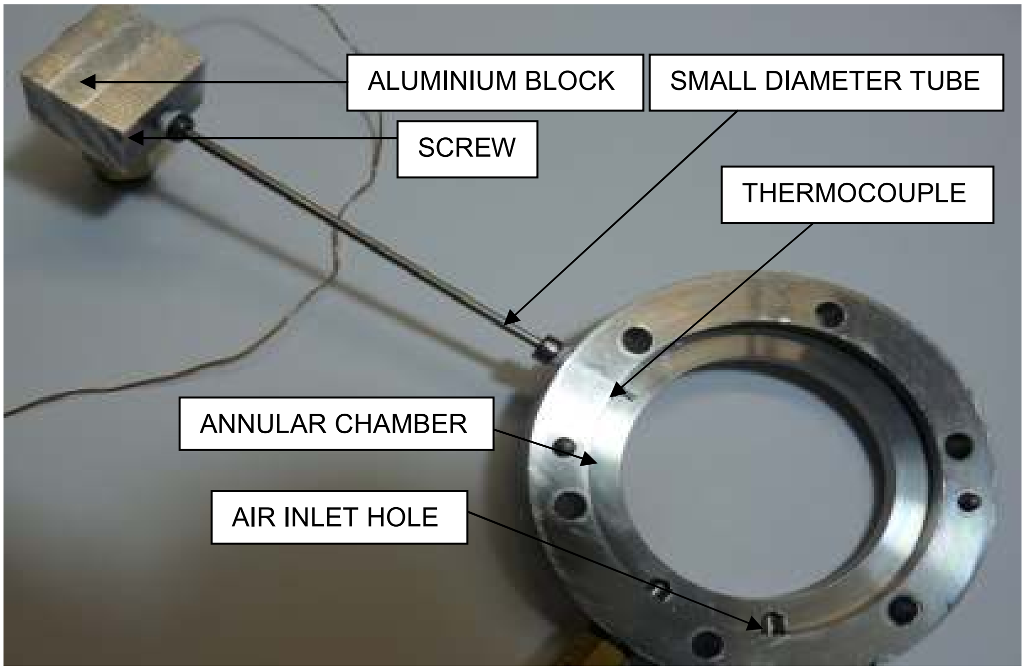

Figure 5.11 Cooling Jacket with instrumentations to measure temperature and pressure

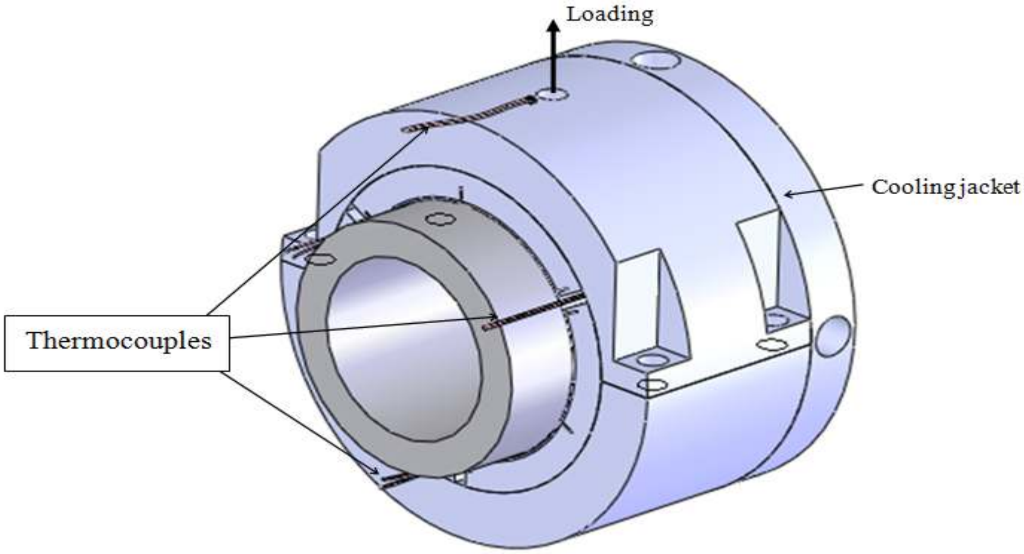

Figure 5.12 Test section and bearing with cooling jacket and thermocouples attached

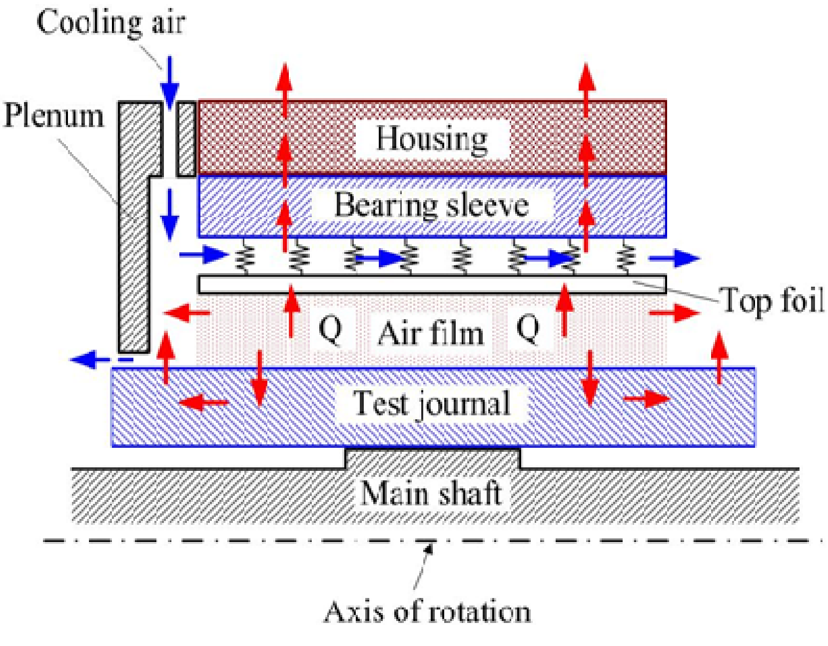

Figure 5.13 Cooling air path (Blue arrows) and heat transfer mechanisms (Red arrows)

5.4 Motor controller parameters

The speed of the motor which drives the test section is controlled by a frequency converter FC 80 from Sieb and Meyer. The operation of the software begins with setting different motor parameters such as rated speed, acceleration rate, deceleration rate as shown in the Figure 5.14. The loaded parameter set is written into the frequency converter and stored.

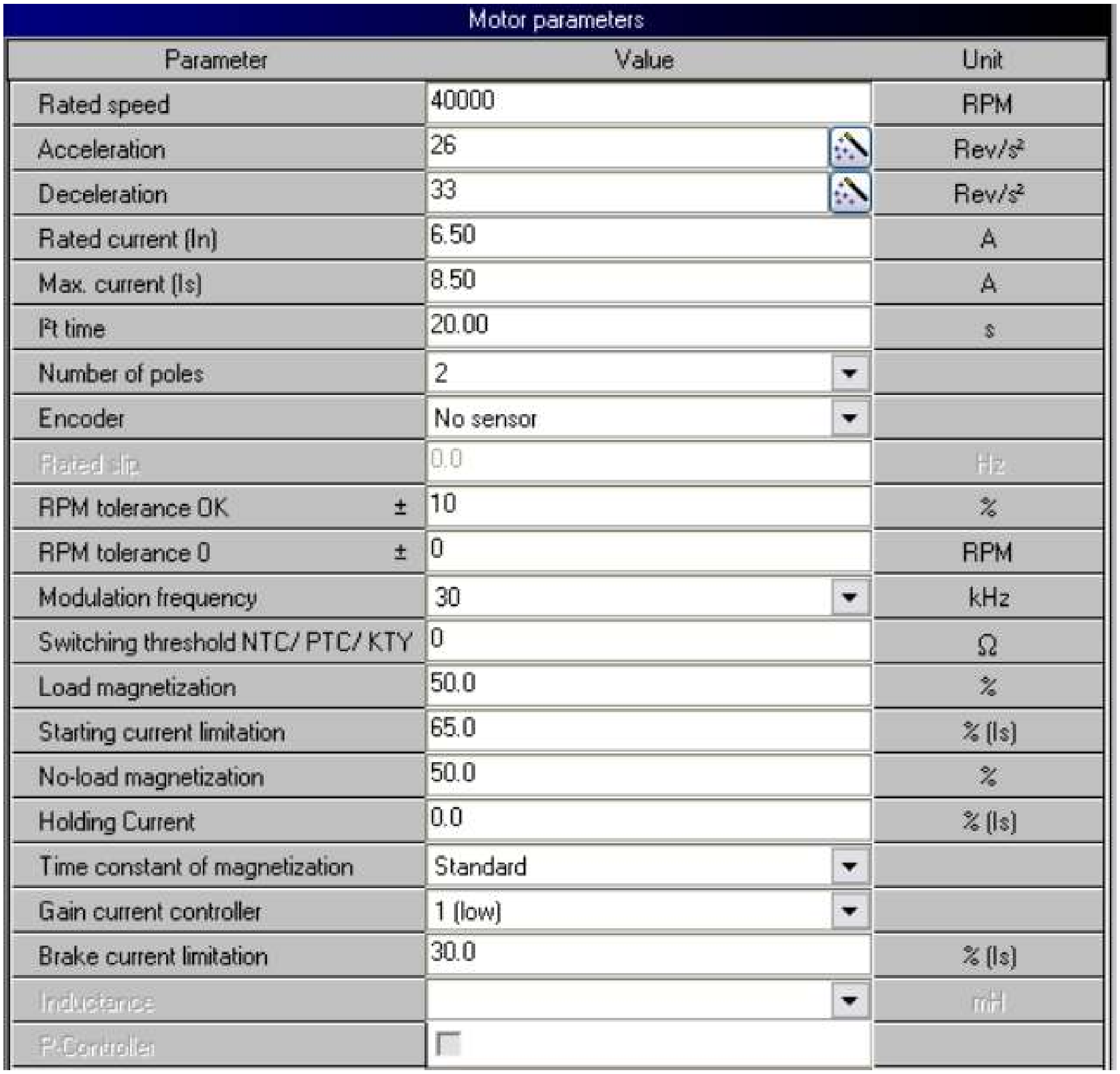

Motor parameters

Parameter	Value	Unit
Rated speed	40000	RPM
Acceleration	26	Rev/s²
Deceleration	33	Rev/s²
Rated current (In)	6.50	A
Max. current (Is)	8.50	A
I^2t time	20.00	s
Number of poles	2	
Encoder	No sensor	
Rated slip	0.0	Hz
RPM tolerance OK ±	10	%
RPM tolerance 0 ±	0	RPM
Modulation frequency	30	kHz
Switching threshold NTC/ PTC/ KTY	0	Ω
Load magnetization	50.0	%
Starting current limitation	65.0	% (Is)
No-load magnetization	50.0	%
Holding Current	0.0	% (Is)
Time constant of magnetization	Standard	
Gain current controller	1 (low)	
Brake current limitation	30.0	% (Is)
Inductance		mH
P-Controller	☐	

Figure 5.14 Motor parameters

On the window “measured values”, the status of the motor is displaced by percentage bars as shown in the Figure 5.15. The current status of the frequency controller is indicated on the top right corner via OK (in green)/ERROR (in red).

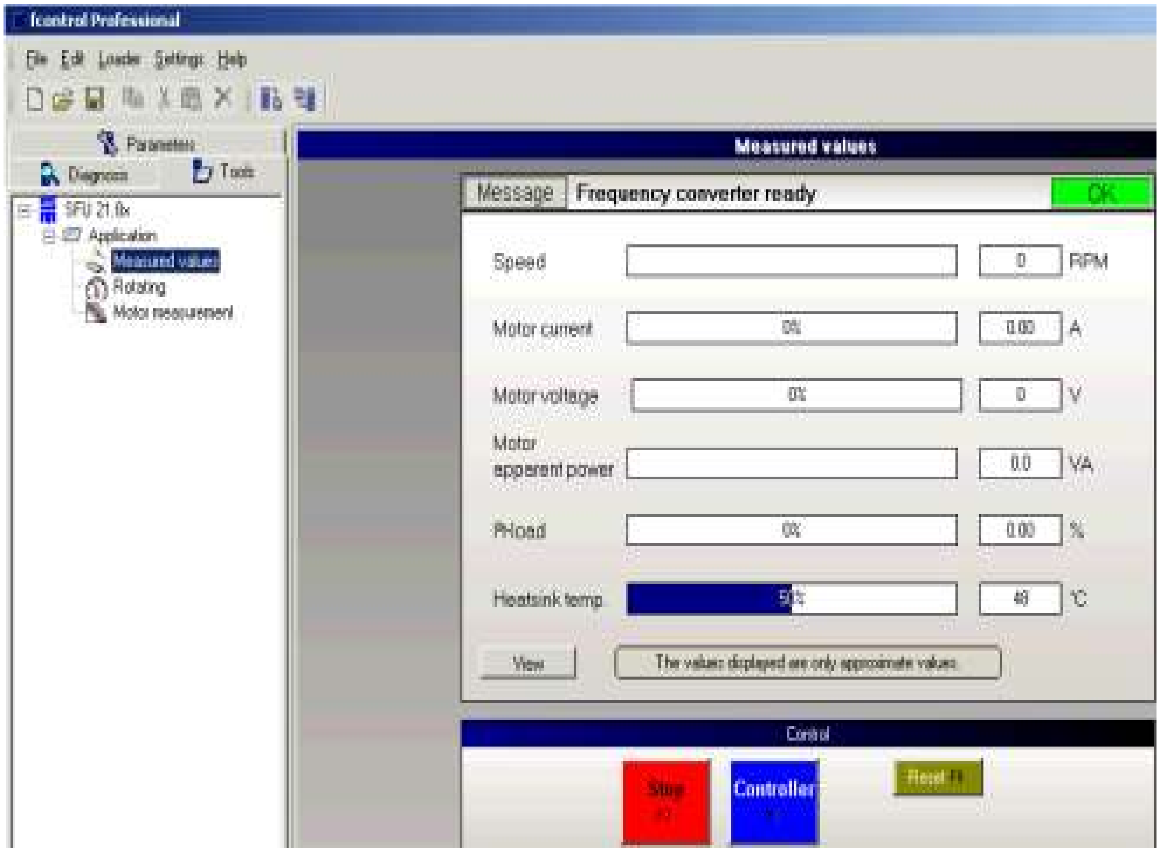

Message: Frequency converter ready — OK

Speed		0	RPM
Motor current	0%	0.00	A
Motor voltage	0%	0	V
Motor apparent power		0.0	VA
Pl-load	0%	0.00	%
Heatsink temp	50%	48	°C

View — The values displayed are only approximate values.

Figure 5.15 Example of the screen that shows status of the motor

The page “motor measurements” parameters of the motor can be adapted to motor by appropriate measurements taken via the tab pages “profiles” and “curves”. In order to test the basic function and the correct direction of rotation, the following parameters should be adjusted during the first test procedure:

- Load magnetization : 50%
- Starting current limitation : 50%
- No load magnetization : 50%

After clicking the controller and start button, the parameters are graphically displayed as shown in the Figure 5.17. The direction of rotation of the motor was made clockwise and its acceleration to desired speed was checked. The parameters were adjusted to

- Load magnetization : 30%
- Starting current limitation : 75%
- No load magnetization : 50%

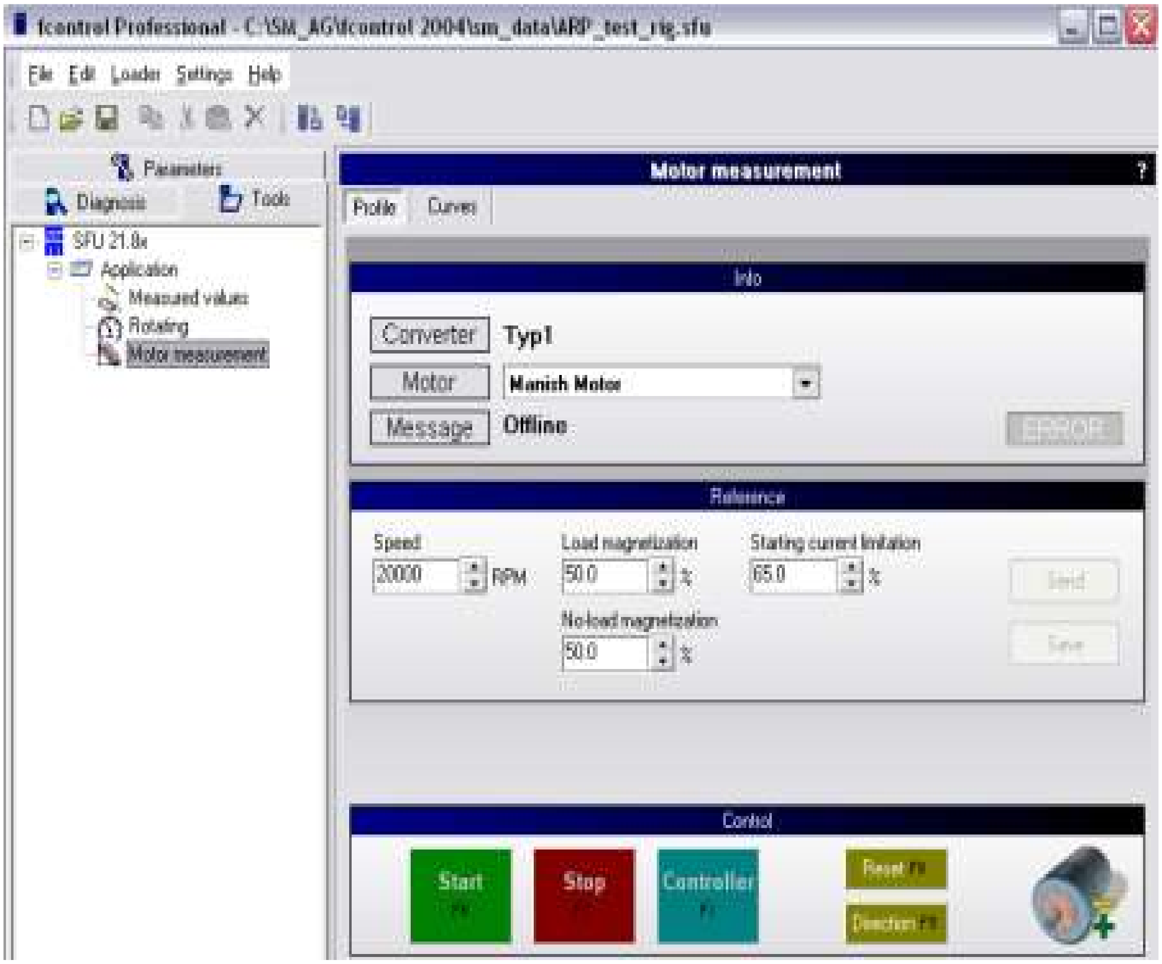

fcontrol Professional - C:\SM_AG\fcontrol 2004\sm_data\ARP_test_rig.sfu

Motor measurement

Info

Converter: Typ1

Motor: Manish Motor

Message: Offline

Reference

Speed: 20000 RPM

Load magnetization: 50.0 %

Starting current limitation: 65.0 %

No-load magnetization: 50.0 %

Figure 5.16 Motor measurement display

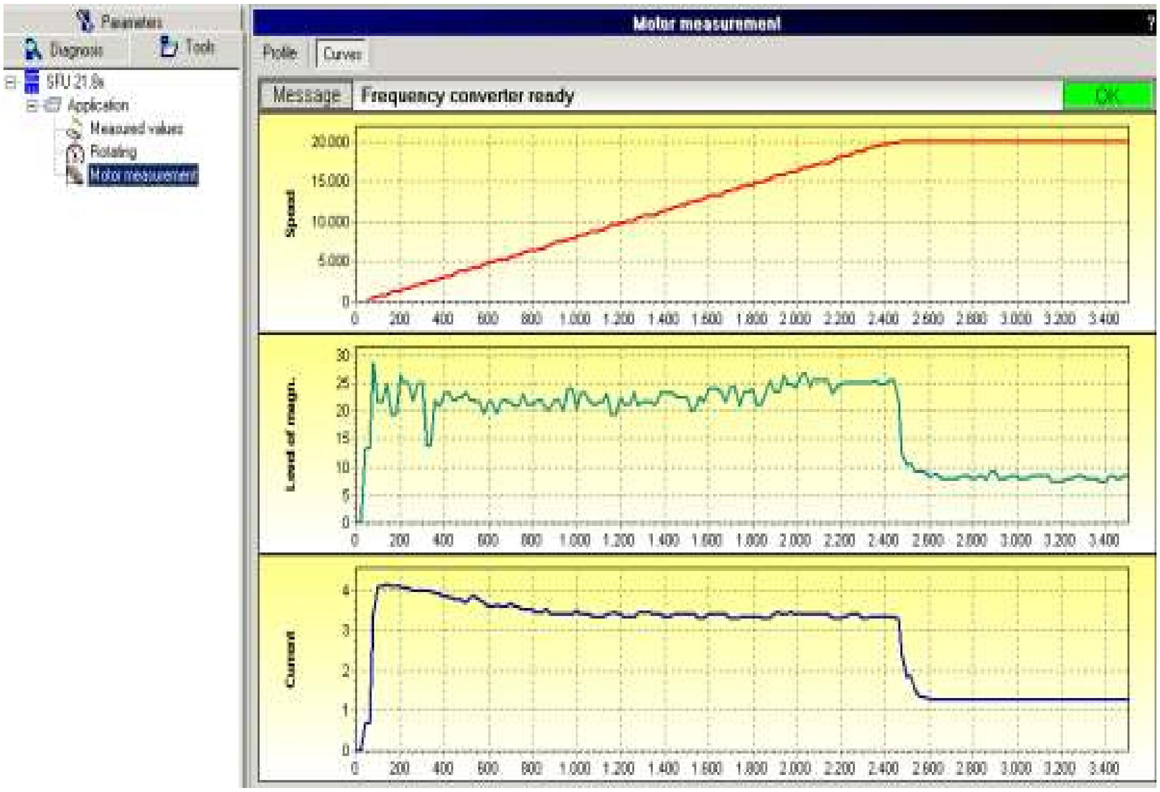

Frequency converter ready

Figure 5.17 Graphical display of parameters

CHAPTER 6

RESULTS AND DISCUSSION

Few preliminary tests were conducted in order to evaluate the uncertainty in the level of measurement. These preliminary tests also were helpful in testing the various thermocouples which were attached. The preliminary tests were conducted at 10lb and 15000 rpm. Fluctuations in temperature values were observed. These fluctuations were due to direct attachment of thermocouple on the top foil. As discussed before, the problem was solved by applying small super glue coating on the top foil and then attaching the thermocouple using the high temperature epoxy.

The test procedure involves speeding up the motor to certain test speed and gradually increasing the load upto certain load and then allowing the test rig to run at that load and the speed until the all the thermocouple readings attain the steady state condition. The thermal time constant is same for every test and independent of speed and load. Therefore, the tests were conducted for approximately 90 minutes until bearing housing reached the steady state conditions.

6.1 Purposes of the experiments

6.1.1 To generate data set to compare with the simulation model

A thermohydrodynamic (THD) model has been developed by other researchers in the lab to experimentally investigate the thermal behavior of the air foil bearings. The experimental data presented in this thesis will be compared with the simulation data from the THD model. The data from this test facility can provide valuable input for bearing development and application.

6.1.2 To investigate break-in characteristics

In typical foil bearing applications, journal is coated with PS304 solid lubricant as shown in Ref [1] or dense chromium. Top foil is coated with Teflon type coating. These coatings help to reduce friction and wears during the start/stop operations. The start-stop cycles act as mild polishing wear mechanism between the asperities of coated top foil and rotor, resulting in smooth surfaces on both top foil and rotor.

In the current test rig, the rotor was coated with 10 micron thick dense Chromium but top foil is bare stainless steel 316 without any coating. The purpose of break-in tests in our experiments is to see if bare top foil is compatible with dense chromium coated shaft.

The break-in characteristics were compared at 22 lb and 35000 rpm for 2 different set of top foils. The first set of top foil shows small break-in peak of about 67˚ C and it disappears immediately as shown in the Figure 6.1. The second set of bearing showed a rapid increase in the temperature due to break-in reaching 150˚ C and then attained the steady state conditions as shown in the Figure 6.2. The test was repeated and the second test did not show the high initial peak. All the subsequent tests presented in this thesis are from the second set of the bearing after the two break-in runs.

This difference in steady state of two different bearings is believed to be due to minute differences in the top foil thickness and other components. In overall, SS 316 showed excellent break-in behavior with dense Chromium coated shaft.

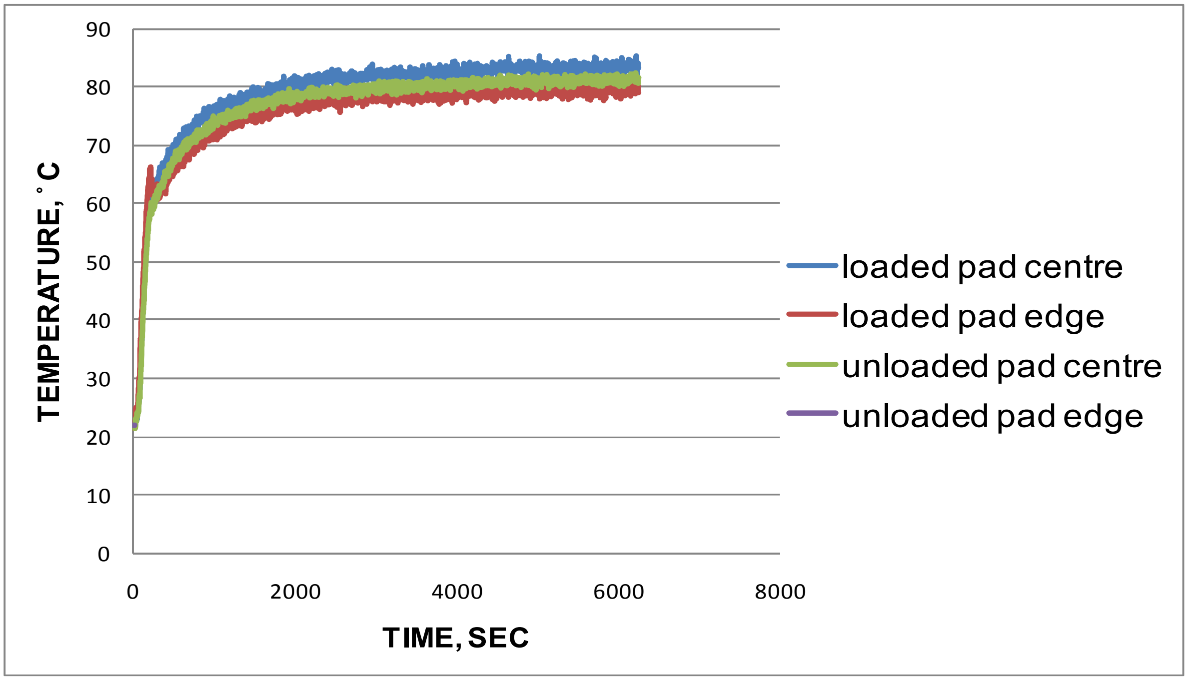

Figure 6.1 Break-in characteristics of the first top foil set at 22lb and 35000 rpm

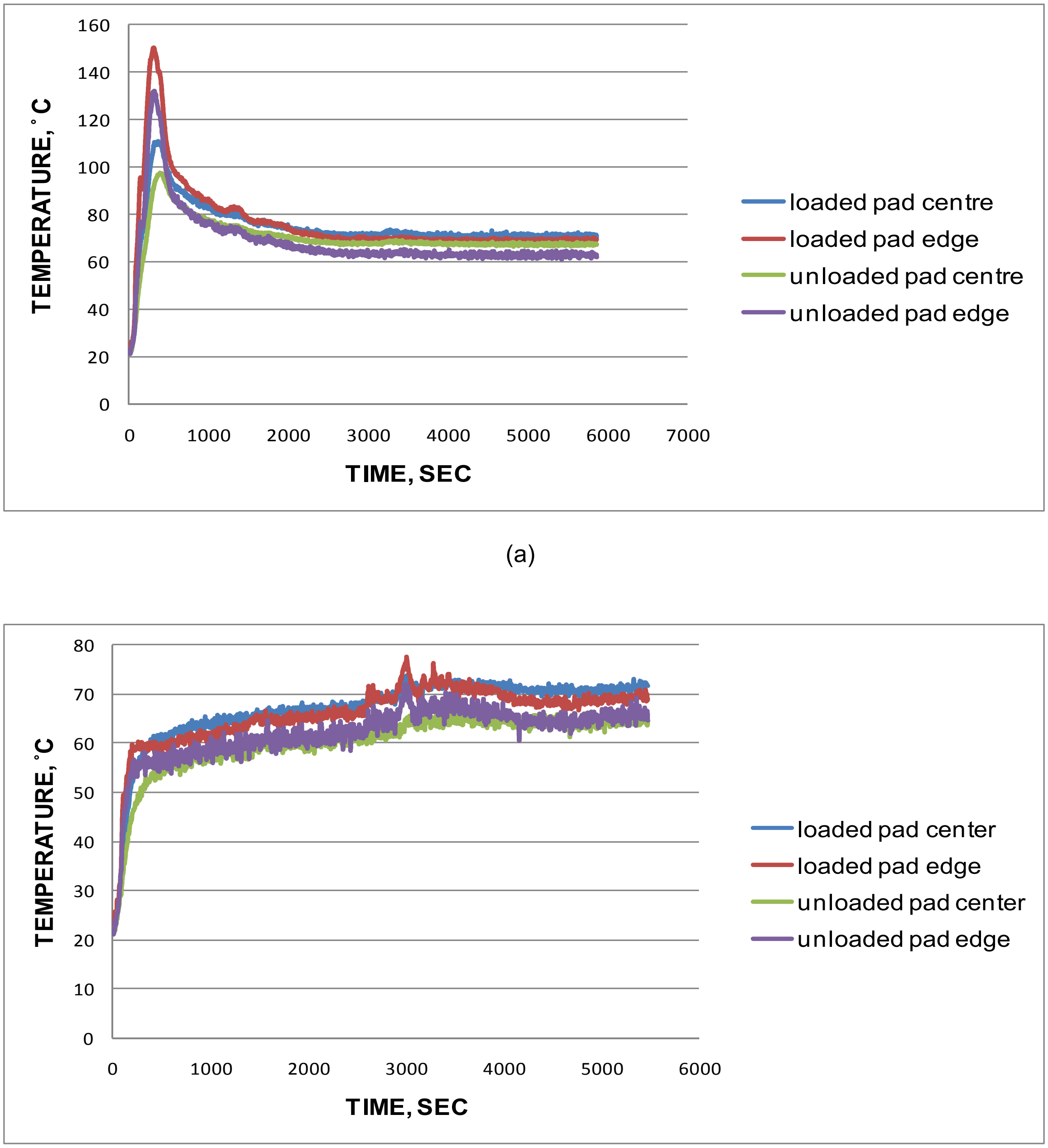

(a)

(b)

Figure 6.2 Break-in characteristics of the second top foil set at 22lb and 35000 rpm (a) first run (b) second run

6.1.3 To find optimal cooling air pressure

At high speeds, thermal and centrifugal growth contributes to significant temperature rise which can eventually lead to thermal instability. As a result appropriate cooling is required at high speeds. Typical method of foil bearing cooling is to pass the cooling air through channels formed by bump foils. One side of the bearing is exposed to high pressure to induce the cooling air flow. Cooling effect increases with supplied pressure. However, providing cooling air requires energy consumption somewhere, and ideal cooling method would be to minimize the amount of cooling air maintaining the bearing thermally stable. One of the purposes of the experiment is to find optimum cooling air pressure for the designed foil bearing.

6.1.4 To find the thermal contact resistance between the bearing sleeve and its holder.

The experimental test results obtained will be utilized to verify a computational simulation code written for THD analysis of air foil bearings by other researchers. To compare the experimental data with simulation model, identification of exact thermal boundary condition is necessary. One of the important thermal boundary condition is the thermal contact resistance between the bearing sleeve and its housing which encloses the bearing sleeve. A simple instrumentation was devised to measure the thermal contact resistance.

6.2 Effect of rotor rotational speed

Temperature distributions were investigated at various speeds. The speeds were increased from 30000 rpm to 40000 rpm keeping the load constant at 12 lb. It can be observed that for a bearing operating at a constant load of 12lb, an increase in rotor speed causes the bearing temperature to rise. It can be seen from the Figure 6.3, increase in speed from 30000 rpm to 40000 rpm resulted in increase of loaded pad center temperature from 60˚ C to 68˚ C. It can also be observed that the loaded pad center temperature is slightly higher than the edge temperature.

An unusual phenomenon was observed for the 12lb and 30000rpm case, wherein there was a temperature jump after the transient period for both loaded and unloaded pad as shown in the Figure 6.3. The same kind of behavior was also observed for the center bearing housing block as shown in the Figure 6.4. The exact reason for this phenomenon is unknown. One plausible explanation is that at 30000 rpm there could have been a ball bearing misalignment problem which resulted in the temperature jump. Even a small change in the operating conditions of ball bearings can produce significant changes.

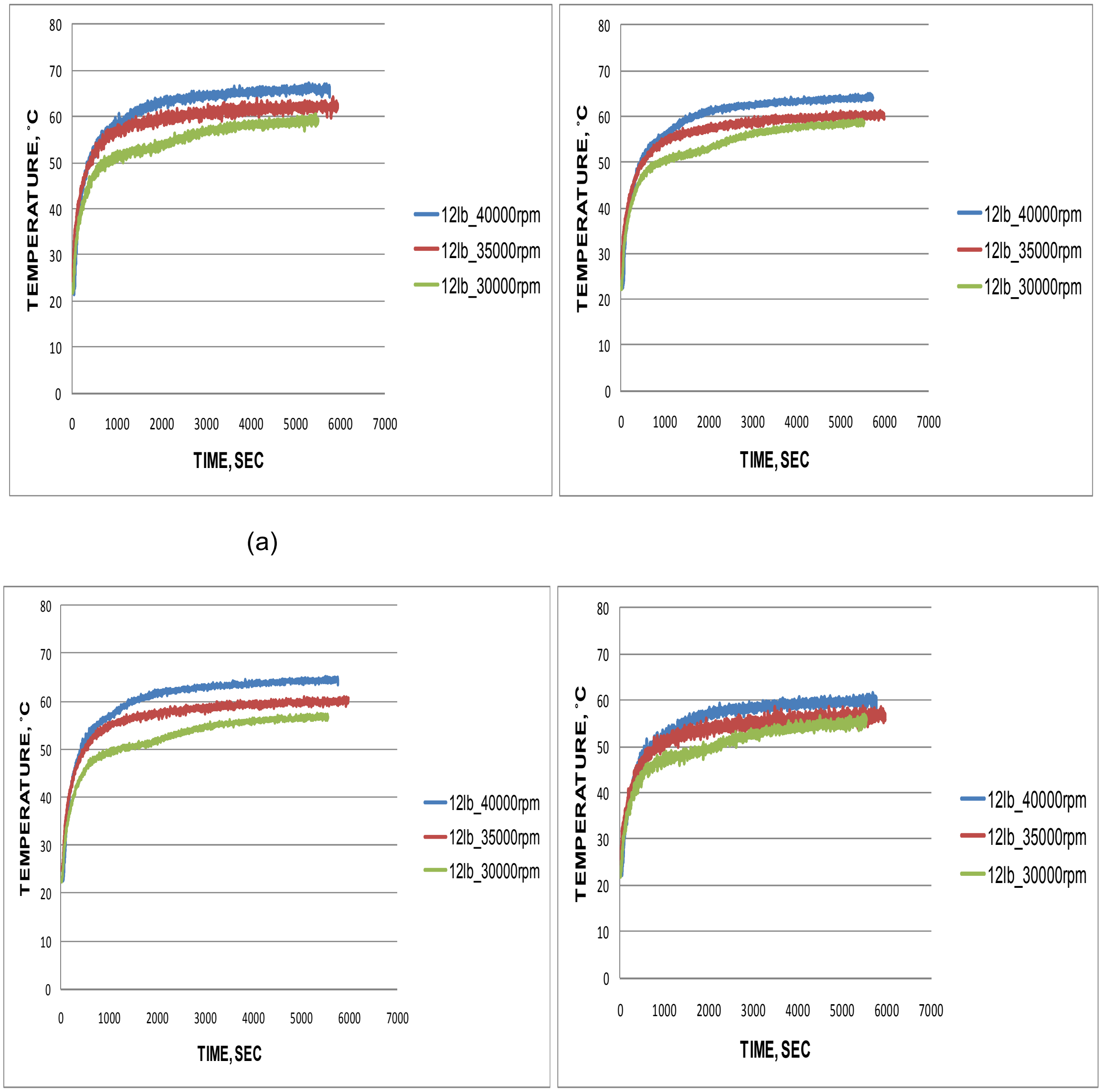

(a)

(c)

(d)

Figure 6.3 Top foil temperatures at same load and different speeds (a) Loaded pad centre temperature (b) Loaded pad edge temperature (c) Unloaded pad centre temperature (d) Unloaded pad edge temperature

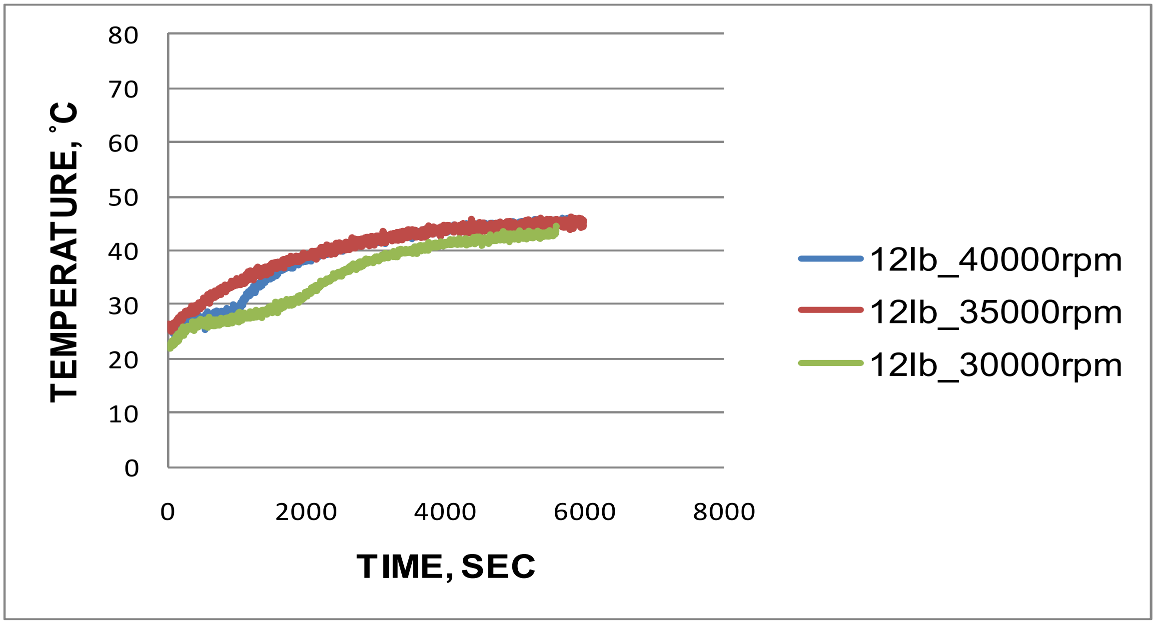

Figure 6.4 Center bearing housing temperature at same load and different speeds

Figure 6.5 shows the ball bearing temperature at 12 lb and different speeds. It can be observed that there is a slight increase of ball bearing temperature with speed. Figure 6.6 shows the bearing holder temperature at same load and different speeds. Similar to ball bearing temperature, bearing holder temperature also increased slightly with speed. Figure 6.4 and Figure 6.7 shows the center and front bearing housing temperature at same load and different speeds. At steady state it was observed that the temperature was almost the same even after increasing the speed from 30000 rpm and 40000 rpm.

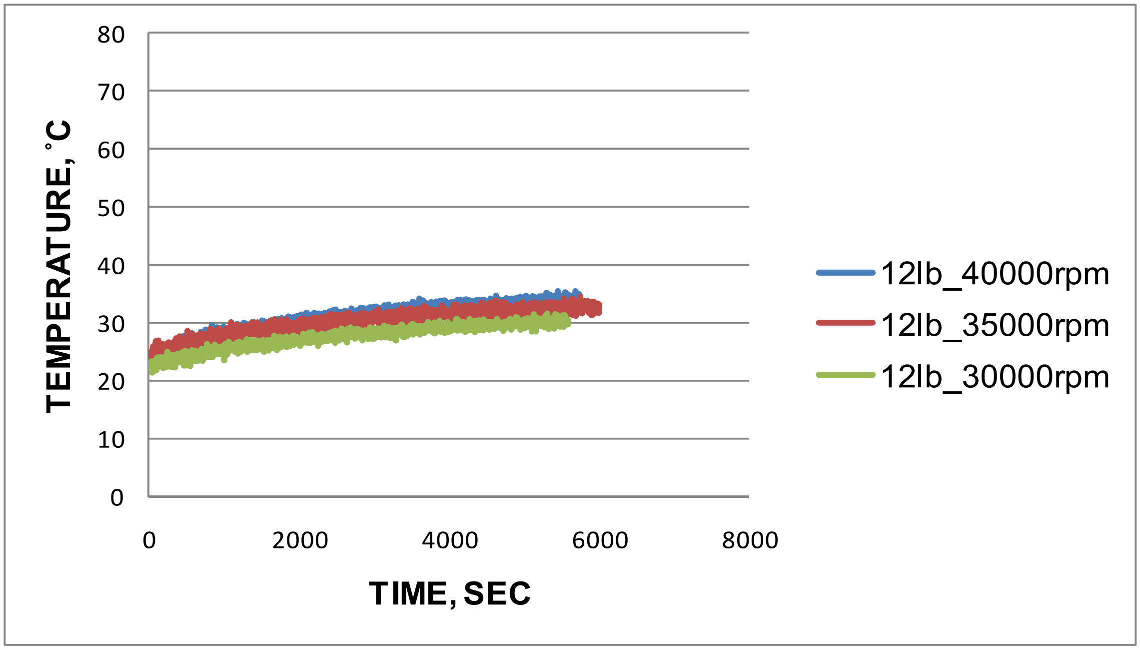

Figure 6.5 Ball bearing temperature at same load and different speeds

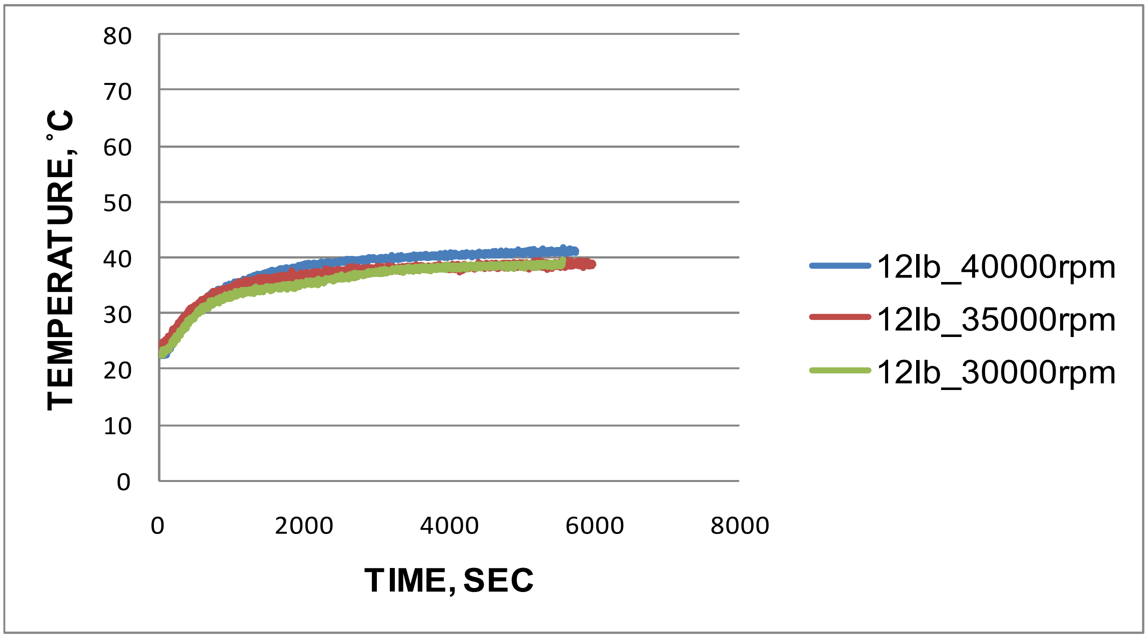

Figure 6.6 Bearing holder temperature at same load and different speeds

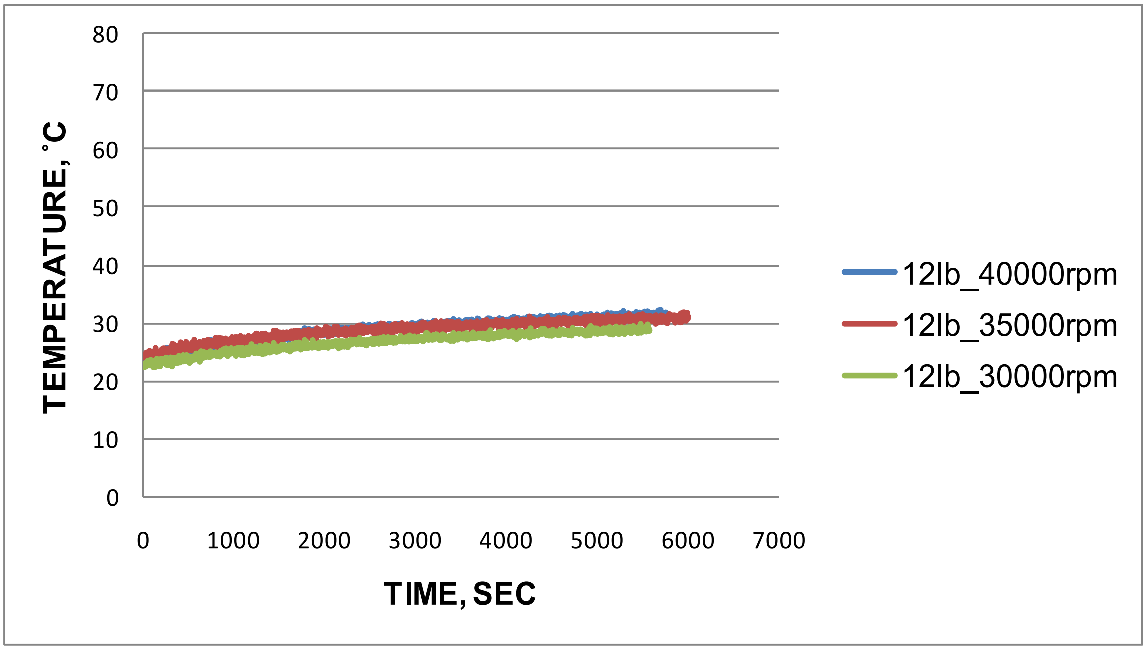

Figure 6.7 Front bearing housing temperature at same load and different speeds

6.3 Effect of external loads

For a bearing operating at a constant speed, increase in the radial load will cause the temperature of the bearing to rise. As the load increases the film thickness reduces, which in turn increases the temperature of the foil structure. At a 22lb load, a sharp rise in top foil edge temperature was observed as shown in the Figure 6.9 . Almost a 10˚ C rise in temperature was observed on the loaded pad when the load was increased from 12lb to 17lb. But increasing the load from 17lb to 22lb did not show much rise in temperature. The ball bearing did not show any rise in temperature when the load was increased from 12lb to 22lb as shown in the Figure 6.10 because ball bearing load capacity is much larger than range of loads applied to the foil bearing. Bearing holder temperature at same speed and different loads is shown in the Figure 6.11. As the load was increased, a slight increase in the bearing holder temperature was observed. The temperature difference (ΔT) between averaged top foil temperature and bearing holder temperature also increases with load, which indicates more heat transfer from top foil to the bearing holder under higher load as shown in the Figure 6.8. Three pad bearings generally have low load carrying capacity because of its small pad arc length. The maximum load that the bearing could take was close to 25lb.

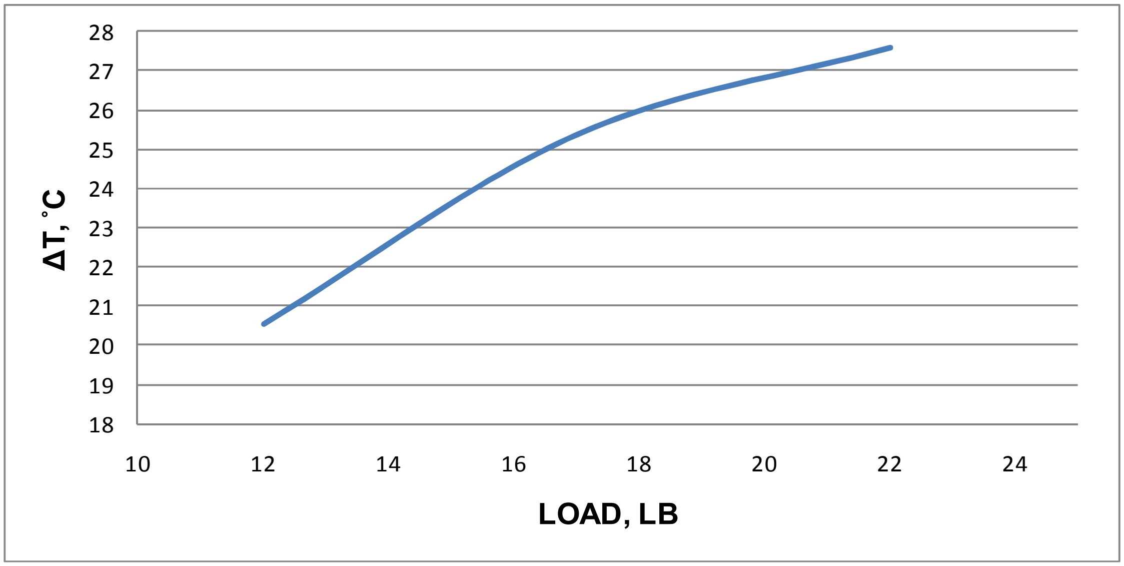

Figure 6.8 Temperature difference V/s Load

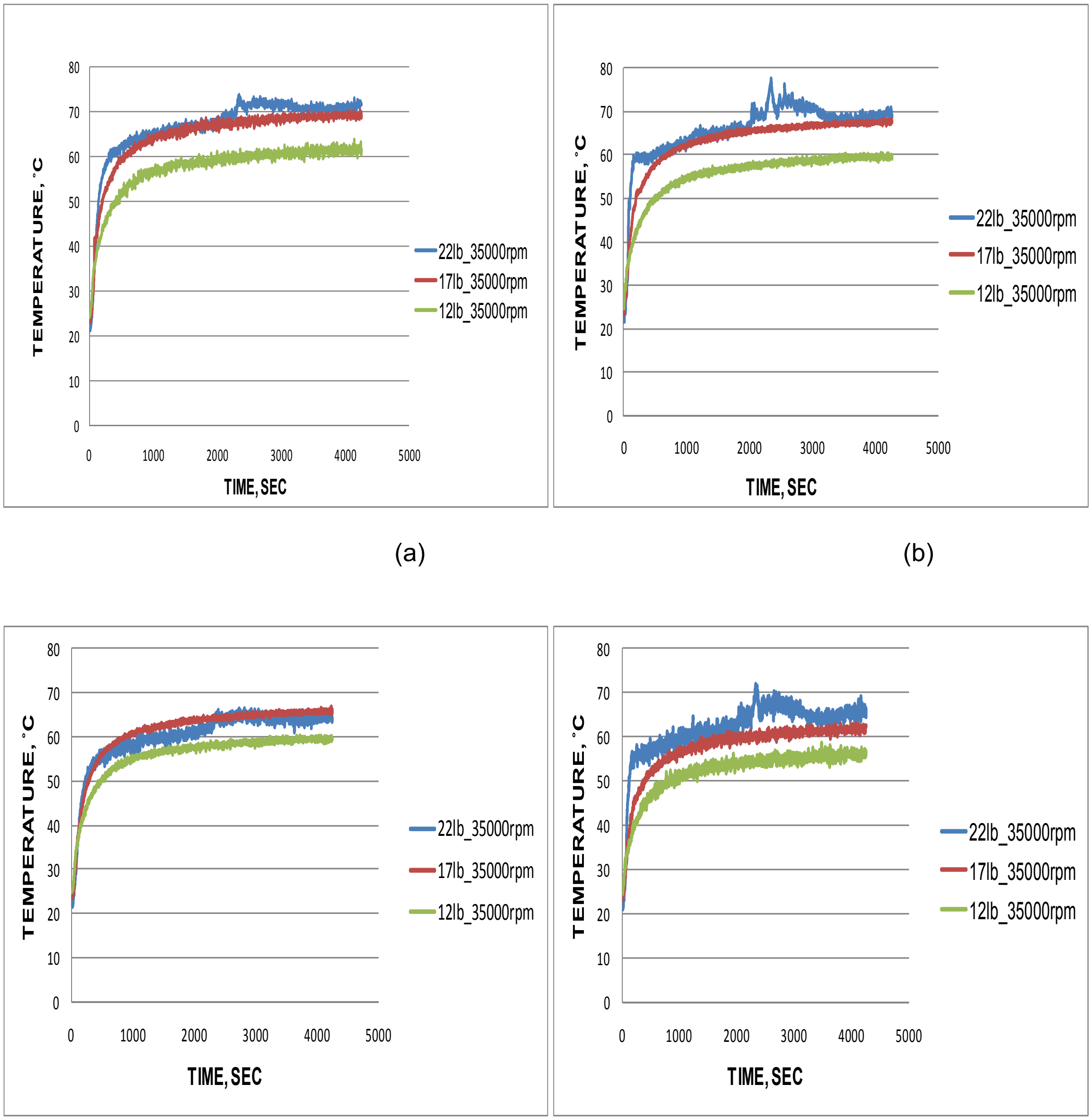

(a) (b)

(c) (d)

Figure 6.9 Pad temperature at different loads and 35000 rpm (a) Loaded pad centre temperature (b) Loaded pad edge temperature (c) Unloaded pad centre temperature (d) Unloaded pad edge temperature

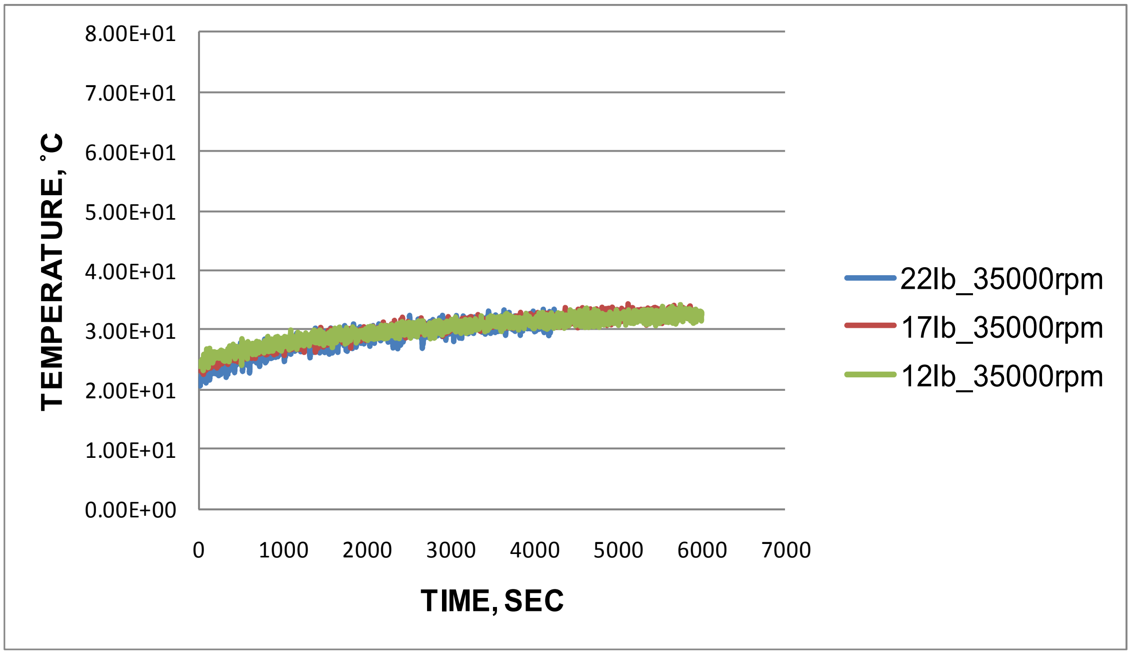

Figure 6.10 Ball bearing temperature at different loads and 35000 rpm

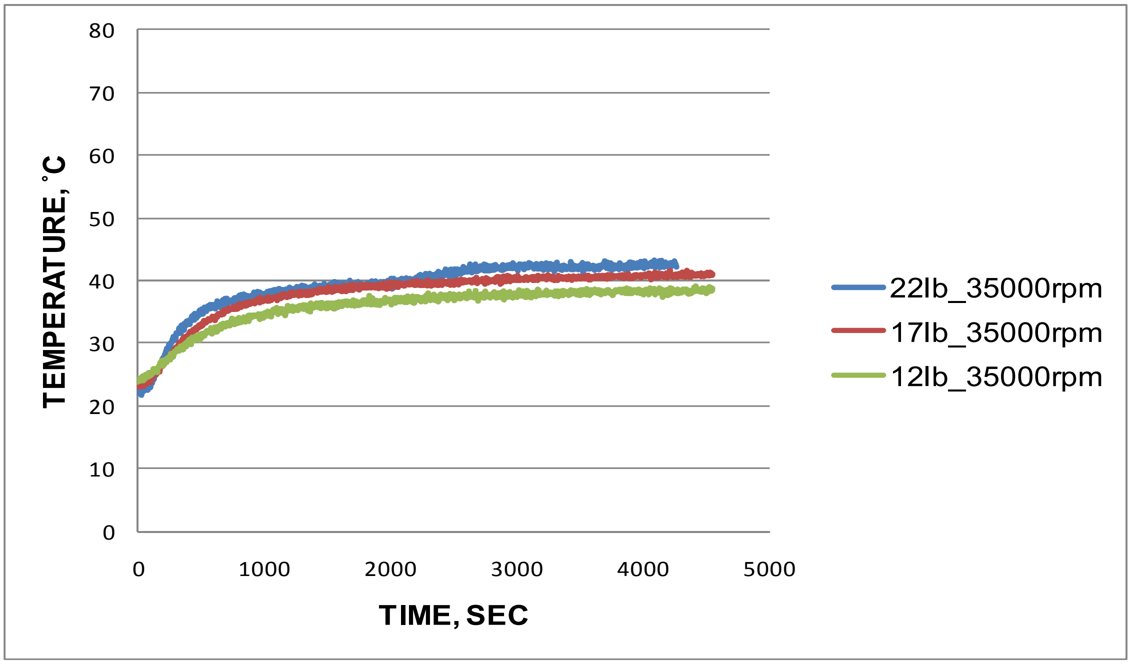

Figure 6.11 Bearing holder temperature at different loads and 35000 rpm

6.4 Effect of cooling air pressure

At high speeds, thermal and centrifugal growth contributes to significant temperature rise. As a result appropriate cooling is required at high speeds. The effect of cooling on temperature was investigated by varying the pressure drop in the bearing. This varying pressure drops results in varying air flow rate through the channels. Figure 6.12 shows the temperature of loaded pad at different pressure drops and also with and without the cooling jacket. The maximum temperature was observed when the cooling jacket was attached but with no cooling air supply. Attaching the cooling jacket at one end partially blocks the escape of hot air and results in recirculation of hot air, which finally leads to significant temperature rise. As the cooling air pressure was increased it was observed that the temperature gradually decreased.

From the Figure 6.12, it is observed that the temperature at 1020 Pa and 1360 Pa was found to be almost the same. One plausible explanation as the cooling air pressure increases; flow speed becomes higher and there is very little time for the cooling air to pick up the heat. This can be clearly observed from the Figure 6.13 which shows a plot of percentage cooling effectiveness versus cooling air pressure.

The cooling effectiveness of the loaded pad edge was more than the loaded pad center because of its proximity to plenum. The percentage of cooling effectiveness for loaded pad edge was almost 2.5 times more than the loaded pad center. So the optimal pressure was considered to be around 1020 Pa which results in maximum cooling effectiveness. The pressures greater than 1020 Pa had almost same effectiveness as that at 1020 Pa. At 12 lb load and 30000 rpm, 16% and 22% reduction in the loaded pad center and edge temperature was observed as the cooling air pressure was increased from 340 Pa to 1360 Pa.

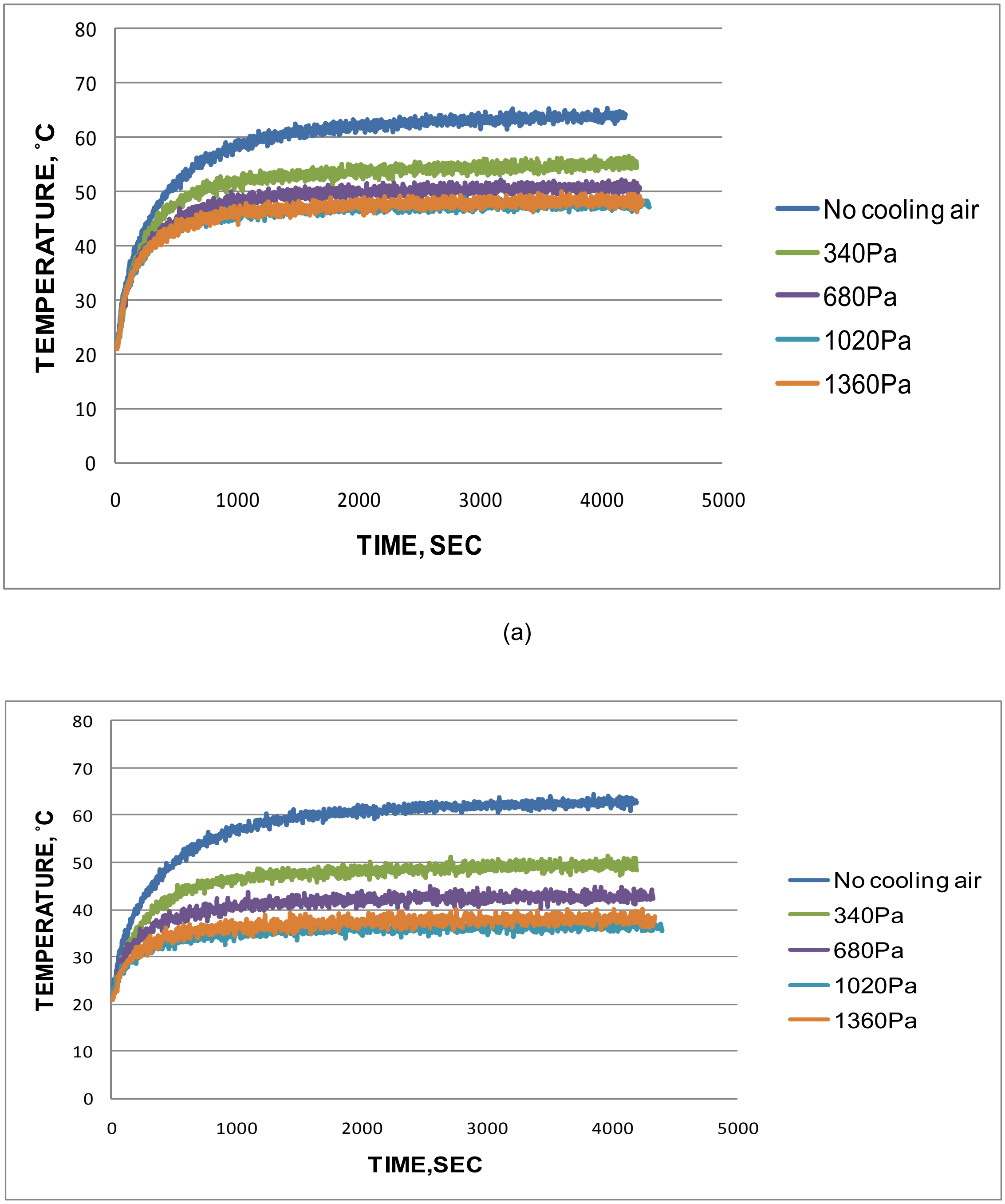

(a)

(b)

Figure 6.12 Loaded pad temperatures at 12lb and 30000 rpm under different air cooling pressures (a) Loaded pad center temperature (b) Loaded pad edge temperature

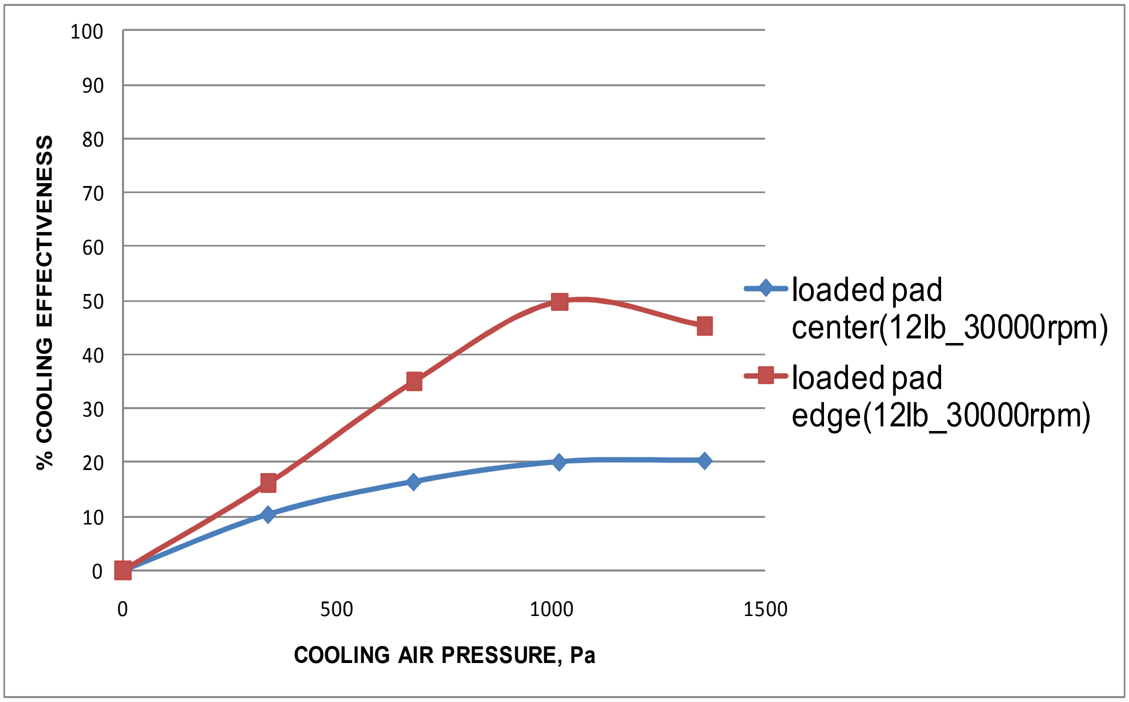

Figure 6.13 Percentage of cooling effectiveness Vs Cooling air pressure

Figure 6.14 also shows the same trend with maximum cooling effectiveness at 1020 Pa and pressure more than that resulted in lower effectiveness or same effectiveness as at 1020 Pa. Figure 6.16 shows the loaded pad temperature at 17lb and 35000rpm under different air cooling pressures. However at 17 lb load and 35000 rpm, a different cooling effectiveness trend was observed. It can be observed from the Figure 6.17 that the cooling effectiveness at 680 and 1020 Pa were almost the same and maximum cooling effectiveness was at 1360 Pa. At 17lb and 35000 rpm, there was 23% reduction in bearing sleeve temperature as the cooling air pressure was increased from 340 Pa to 1360 Pa as seen in the Figure 6.18.

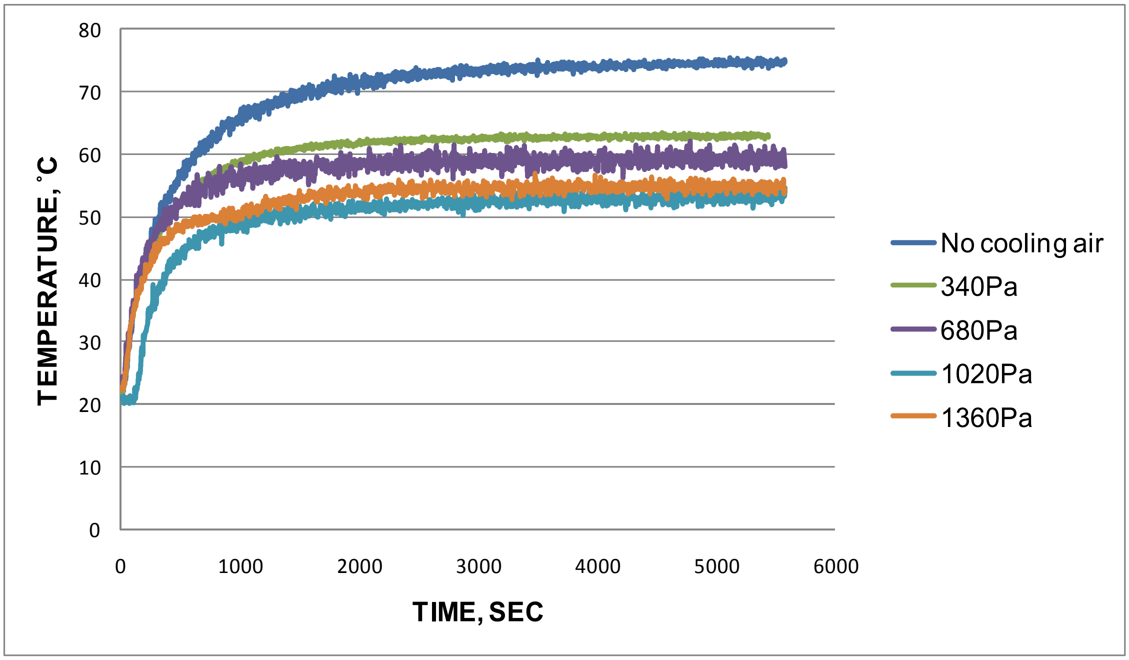

(a)

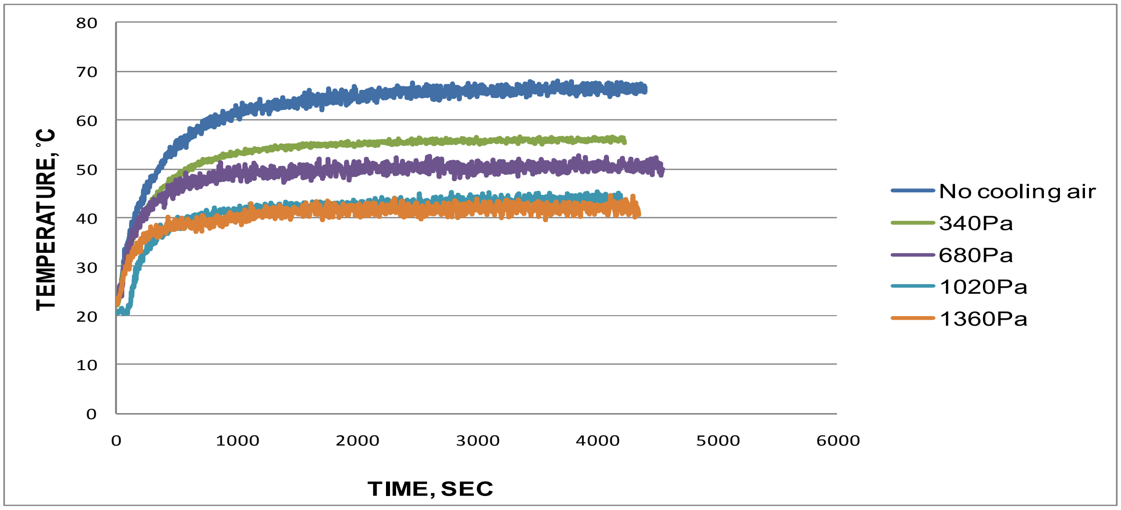

(b)

Figure 6.14 Loaded pad temperatures at 12lb and 35000 rpm under different air cooling pressures (a) Loaded pad center temperature (b) Loaded pad edge temperature

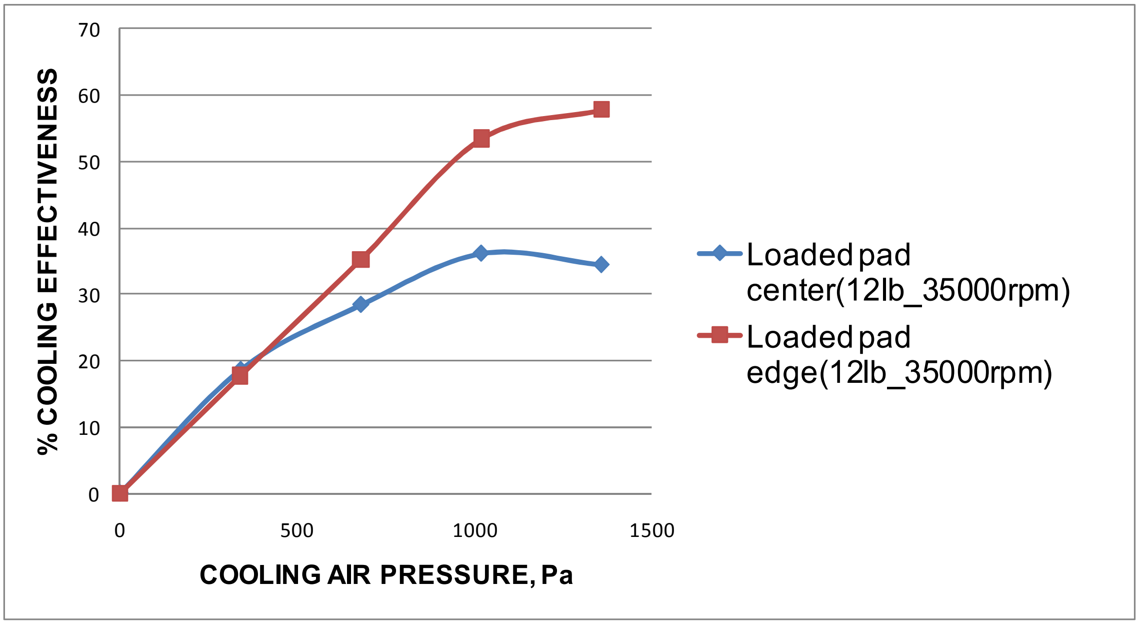

Figure 6.15 Percentage of cooling effectiveness Vs Cooling air pressure

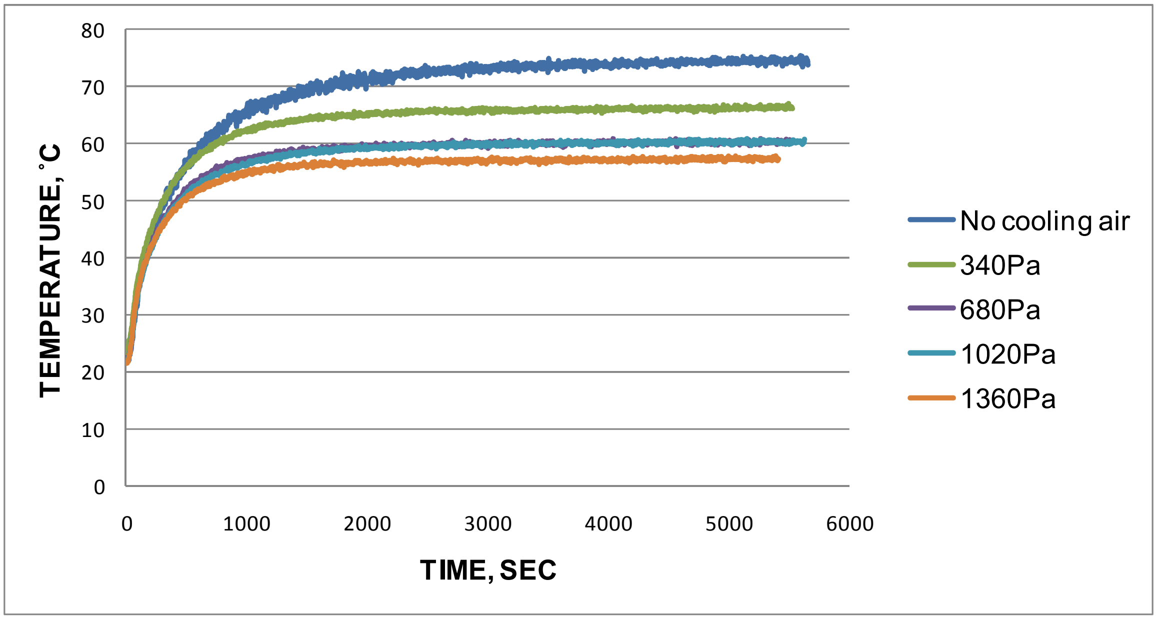

(a)

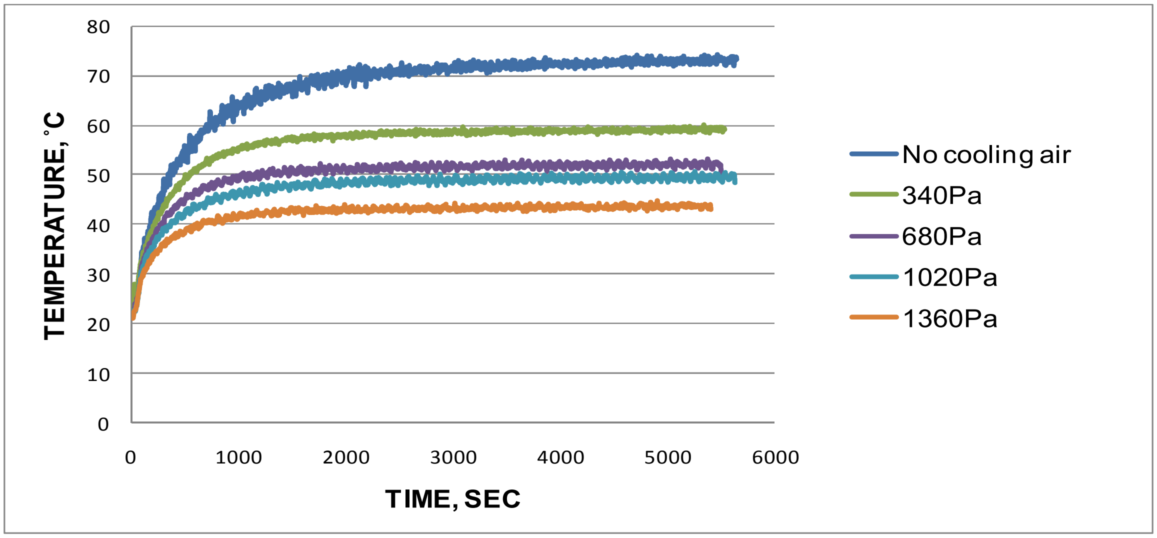

(b)

Figure 6.16 Loaded pad temperature at 17lb and 35000rpm under different air cooling pressures
(a) Loaded pad center temperature (b) Loaded pad edge temperature

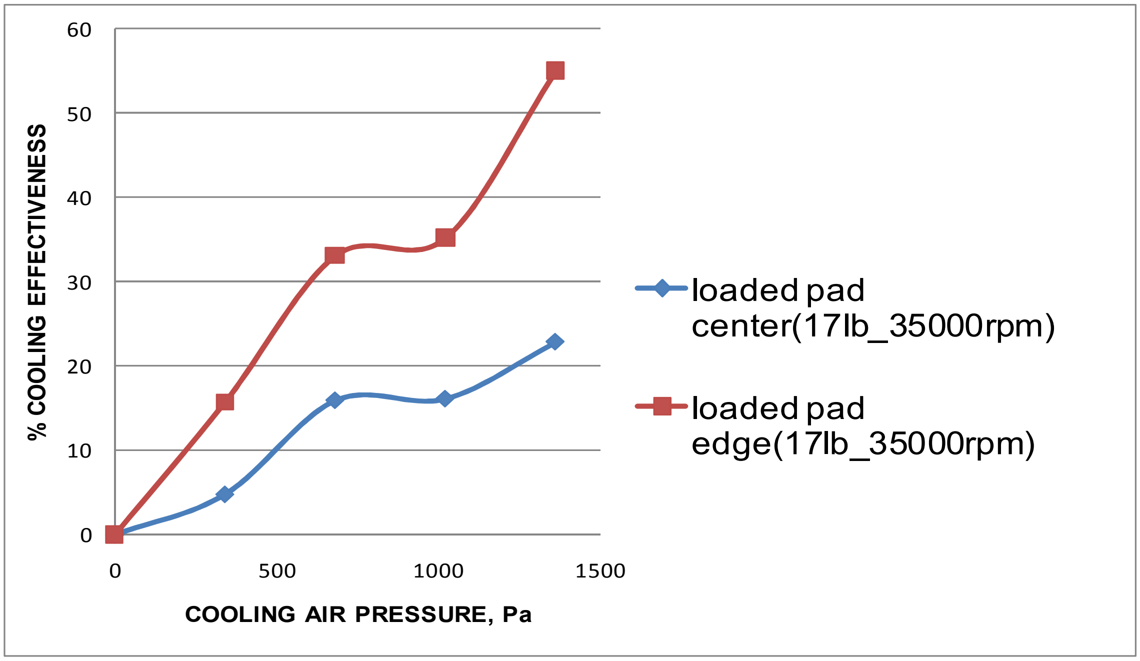

Figure 6.17 Percentage of cooling effectiveness Vs Cooling air pressure

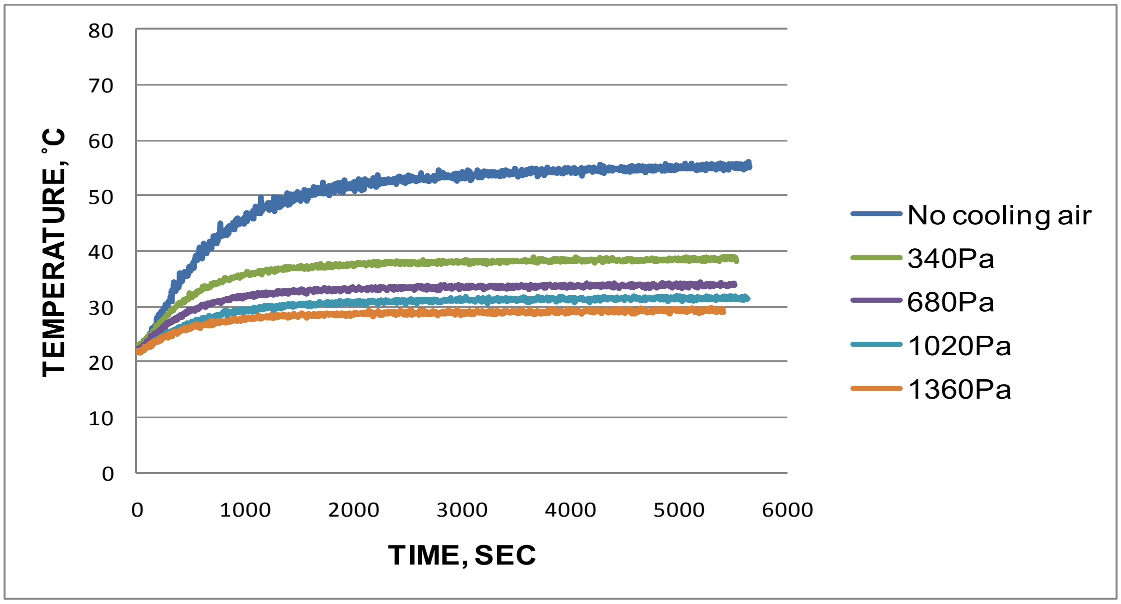

Figure 6.18 Bearing sleeve temperature at 17lb and 35000rpm

6.5 Determination of Reynolds Number across the primary and secondary channels for different cooling air pressure

Reynolds number gives the measure of the type of flow i.e. laminar or turbulent across the channel. To calculate the Reynolds number, cross sectional area of the channel and hydraulic diameter is determined. The hydraulic diameter is found using

$$D = \frac{4A}{P} \tag{10}$$

At 50˚ C which is the steady state temperature of bearing, average viscosity and density values of air are calculated. From these values the mass flow rate of the cooling air was determined for different pressures using

$$m = -\frac{\rho D^2 A}{32\mu}\frac{dp}{dz} \tag{11}$$

Where m is the mass flow rate, ρ is the average density, D is the hydraulic diameter and A is the cross-sectional area of the channel, P is the wetted perimeter and μ is the average viscosity of the air. The pressure at one end of the bearing is at atmospheric pressure and at the other end pressure is sum of the cooling air pressure and the atmospheric pressure. From the mass flow rate, flow velocity is calculated using

$$m = \rho A V \tag{12}$$

Where V is the flow velocity. From this Reynolds number is calculated using

$$\mathrm{Re} = \frac{\rho V D}{\mu} \tag{13}$$

For the simplicity of the problem, the following assumptions are used for the air flow through the channels. The channel cross-sectional area is constant. This assumption is valid while bump deflection is within the elastic limit of the material. The cooling air flow is incompressible and local air density follows the ideal gas law. Viscous heat dissipation and conduction within the air stream are negligible in the cooling channel.

The parameters used for Reynolds number calculation for both the channels at 340 Pa cooling air pressure is shown in the Table 6.1 and Table 6.2. The Reynolds number for different cooling air pressures of the both the channels is shown in the Table 6.3. It can be observed from Table 6.3 that flow is laminar under various cooling air pressures in both the channels.

Table 6.1 Parameters used for Reynolds number calculation of primary channel

Primary channel		
Cross sectional area	A (m^2)	1.06E-06
Perimeter	P (m)	9.33E-03
Hydraulic diameter	D (m)	0.000454448
Absolute Pressure(left side)	P (Pa)	101325
gauge pressure	P (Pa)	340
Absolute Pressure(right side)	P (Pa)	101665
Average pressure	P_{avg} (Pa)	101495
Gas constant	R (J/kg-K)	287
Temperature	T (K)	323
Viscosity	μ (N-s/m2)	1.98E-05
Density	ρ (Kg/m3)	1.094864133
Pressure difference	dp (Pa)	340
Length	dz (m)	3.75E-02
mass flow rate	ṁ (kg/s)	3.42632E-06
Velocity	V (m/s)	2.952313324
Reynolds number	**Re**	**74.11450939**

Table 6.2 Parameters used for Reynolds number calculation of secondary channel

Secondary channel		
Cross sectional area	A (m^2)	1.25E-06
Perimeter	P (m)	6.22E-03
Hydraulic diameter	D(m)	0.000803859
Absolute Pressure(left side)	P (Pa)	101325
gauge pressure	P (Pa)	340
Absolute Pressure(right side)	P (Pa)	101665
Average pressure	P_{avg} (Pa)	101495
Gas constant	R (J/kg-K)	287
Temperature	T (K)	323
Viscosity	μ (N-s/m2)	1.98E-05
Density	ρ (Kg/m3)	1.094864133
Pressure difference	dp (Pa)	340
Length	dz (m)	3.75E-02
mass flow rate	ṁ (kg/s)	1.26422E-05
Velocity	V (m/s)	9.237474662
Reynolds number	**Re**	**410.1941463**

Table 6.3 Reynolds number for different cooling air pressure for both the channels

Cooling air pressure	**Reynolds number in primary channel**	**Reynolds number in secondary channel**
340 Pa	74.11	410.19
680 Pa	148.4	821.7
1020 Pa	223.08	1234.7
1360 Pa	297.94	1649

6.6 Thermal Instability

During the bearing operation, internal temperature is dependent on heat generated by the viscous shearing in the thin air film. At high speeds, the temperature rise of the air film can be significant due to small heat capacity of air. This operation continues and gradually increases the rotor/bearing temperatures causing thermal runaway (thermal instability). The thermal instability was observed at 32 lb and 35000 rpm as shown in the Figure 6.19. It can be observed that the top foil temperature keeps on increasing without attaining the steady state conditions. Thermal instability resulted in damage to the top foil and minor abrasive wear mark on the shaft as shown in the Figure 6.20 and Figure 6.21.

One noticeable feature of the temperature curve is that edge temperature is higher than center temperature unlike all other cases when the bearing is thermally stable. From this experiment, one possible mechanism of thermal instability can be derived; when uniform bump stiffness is used and external load is high, film thickness at the bearing edge is very small because the bearing edge is at ambient pressure and cannot take much load. Air film is trapped inside the bearing and hot air cannot escape the bearing easily. The large recirculation of hot air combined with very small film thickness at the edge may accelerate the temperature rise of the edge. One possible approach to increase the load capacity of the bearing and avoid the thermal instability might be tailoring the bump stiffness distribution, i.e., increase the stiffness at the bearing center but reduce it at the bearing edge.

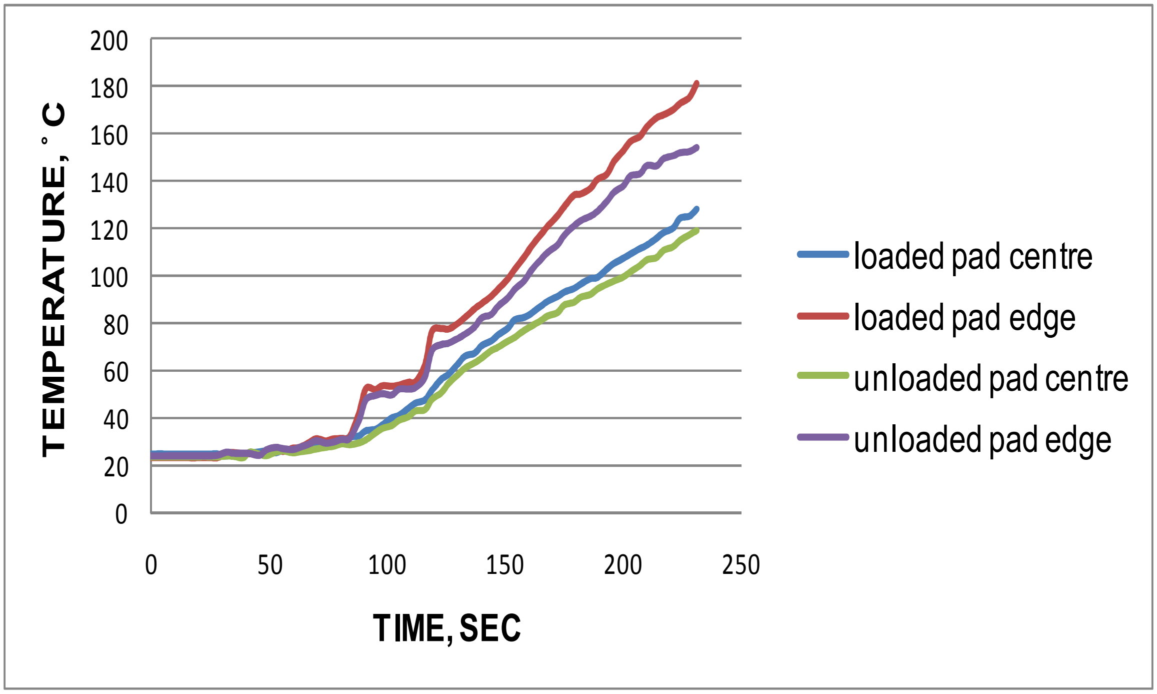

Figure 6.19 Thermal Instability Investigated at 32lb and 35000 rpm conditions

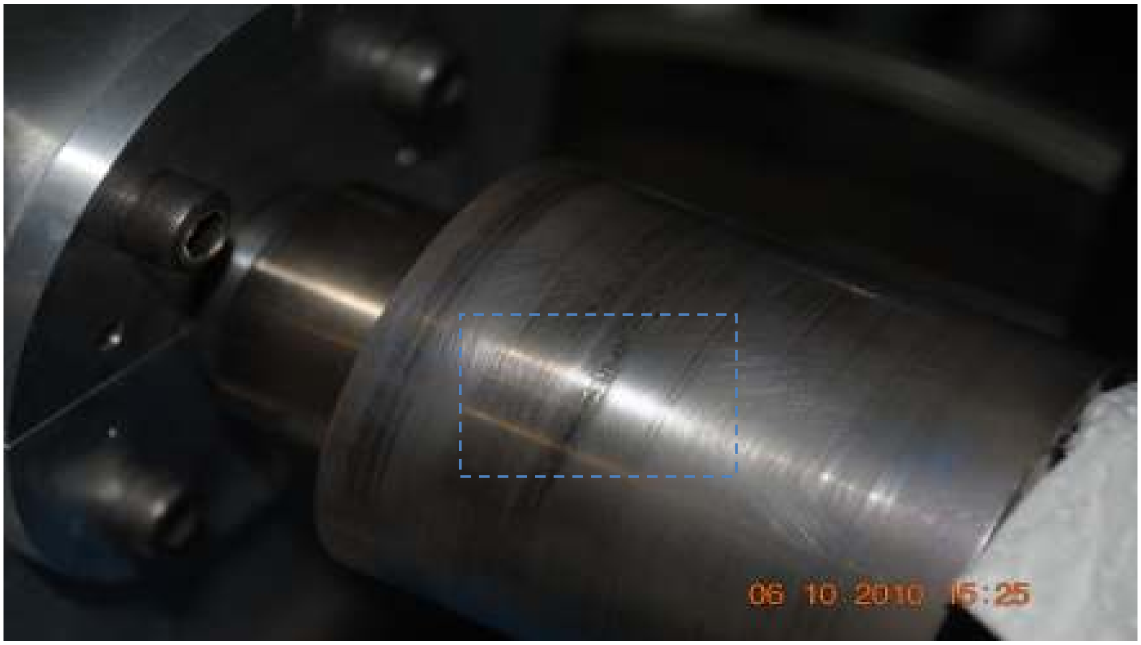

Figure 6.20 Picture showing minor abrasive wear on the rotor

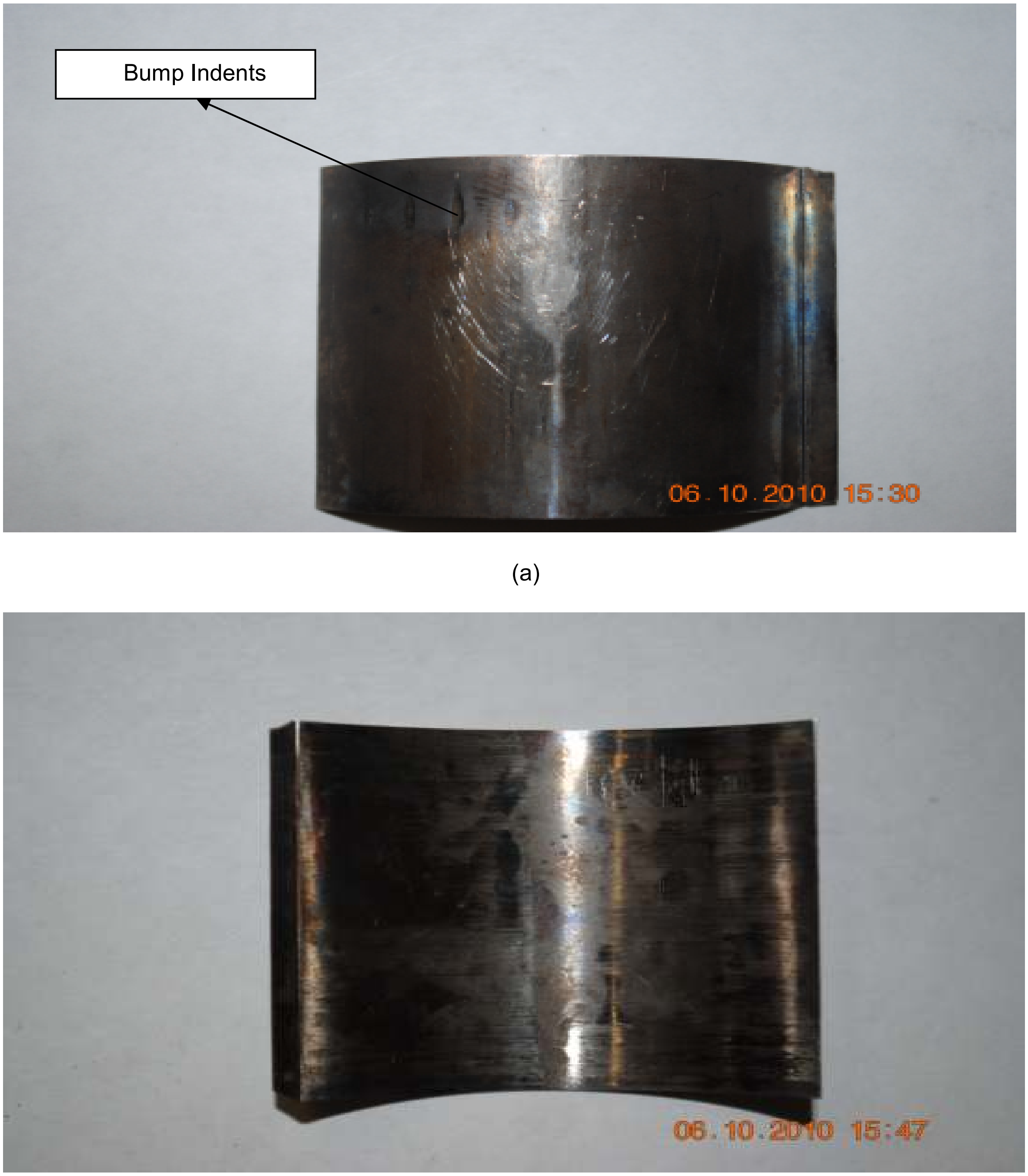

(a)

(b)

Figure 6.21 Picture showing top foil surface damage (a) Outer surface (b) Inner surface

6.7 Determination of Thermal contact resistance between bearing sleeve and its housing

The experimental test results obtained will be utilized to verify a computational simulation code written for thermohydrodynamic analysis of air foil bearings by other researchers. To compare the experimental data with simulation model, identification of exact thermal boundary condition is necessary. One of the important thermal boundary condition is the thermal contact resistance between the bearing sleeve and its housing which encloses the bearing sleeve. Experimental work has been carried in order to measure the thermal contact resistance. A simple instrumentation as shown in the Figure 6.22 was designed to measure the thermal contact resistance between the bearing sleeve and its housing. Two flexible silicone-rubber heat strips (2 inch X 5 inch) were used to provide constant heat to the bearing holder which covers the bearing sleeve. Heavy Insulations were wrapped circumferentially and in the side directions (not shown in the figure) to prevent the heat loss in radial and axial directions. Two thermocouples were used out of which, one was attached on the inner surface of the bearing sleeve and other on the outer surface of the bearing holder. The thermal contact resistance is calculated using the formula,

$$Q = \frac{\left(T_2 - T_1\right)}{\frac{\ln \frac{R_3}{R_2}}{2\pi L K_s} + \frac{\ln \frac{R_2}{R_1}}{2\pi L K_I} + \frac{R_c}{2\pi R_2 L}}$$

Where T_2 and T_1 are the outer surface temperature of bearing holder and inner surface temperature of bearing sleeve respectively, R_1, R_2, and R_3 are inner radius of the bearing sleeve, outer radius of bearing sleeve and outer radius of bearing holder respectively as shown in the Figure 6.23, K_s and K_I are the thermal conductivity of steel and inconel respectively, R_c, Q and L are thermal contact resistance, heat input from the heater and length of the bearing respectively. Q is calculated using formula V^2 / R where V is the voltage and R is the resistance. The values obtained from the experiment are T_2 = 62˚ C, T_1 = 60˚ C, V = 5Volts, and R = 12.25Ω. Taking the values of K_s, K_I, L as 15.26 W/m^2 – K, 11.405 W/m^2 – K and 37.5 mm respectively, we get the value of R_c as 0.00613 K-m^2/W

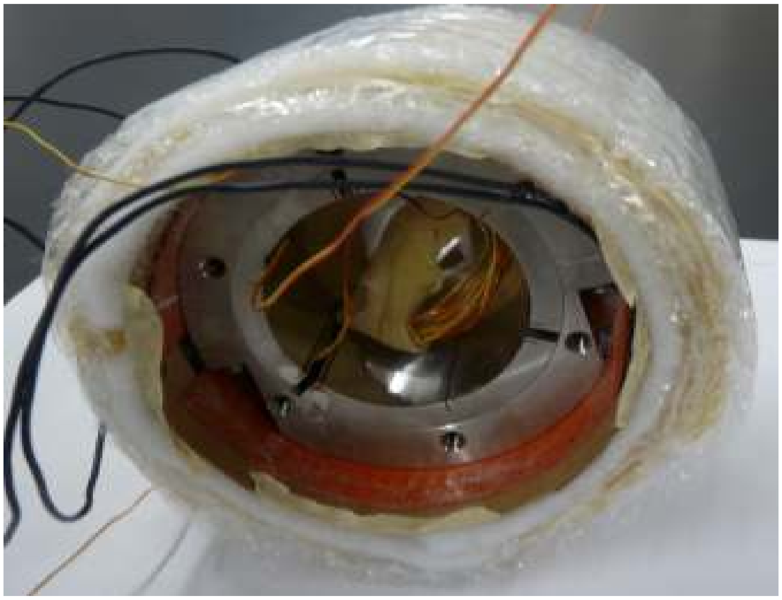

Figure 6.22 Photo of test instrumentation to measure the thermal contact resistance

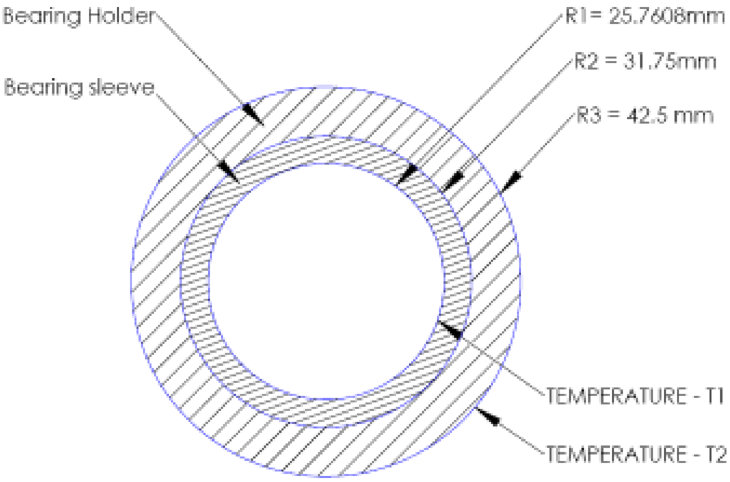

Figure 6.23 Schematic drawing of bearing sleeve and bearing holder

CHAPTER 7

FUTUREWORK

Present experiments were carried out at room temperature with bearing cooling using axial flow through the bump foils. Tests were performed up to only 40,000 rpm due to small torque of the drive motor.

Future works includes

7.1 Tests at high temperature environment

Future testing can be done at very high ambient temperature using the high temperature furnace. At high temperature, the effect of rotor growth on thermal behavior of the bearing can be investigated. Load capacity variations with the temperature can also be measured. It will also be interesting to monitor not only the temperature but the viscous torque generated by the bearing during the load capacity tests.

7.2 Tailoring the stiffness distribution along the axial direction

Tailoring the stiffness distribution of the bearing is another work which can be done in future to determine the variation of load carrying capacities with stiffness. As said earlier, bump stiffness is uniform for the present experimentation. So in future stiffness is tailored in such a way that bearing has very high stiffness at the center than at the edges.

7.3 Testing at hybrid mode

The present test was completely done in hydrodynamic mode. Testing can be further extended to hybrid mode (hydrodynamic + hydrostatic) by supplying the externally pressurized air into the bearing clearance. Bearing friction torque and load carrying capacity can be measured under the hybrid conditions. Bearing thermal behavior can also be investigated under hybrid operation.

7.4 Testing with a new motor drive

The present motor of the test rig was not capable of generating enough torque at high speeds and loads. So in future a new motor drive can be used to run the test at very high speeds and very high loads. Various performance characteristics can be measured at these high speeds and loads. Temperature distributions in the bearing can be investigated at high speed and load conditions.

7.5 Rotor cooling and radial injection of cooling air

Future work also includes rotor cooling and radial injection of cooling air into the bearing to determine the cooling effectiveness. In radial cooling method, supply air passed through the radial holes provided on the bearing sleeve as shown in the Figure 7.1 and Figure 7.2. Both axial and radial cooling methods can be compared to see which is more effective in bring down the temperature of the bearing.

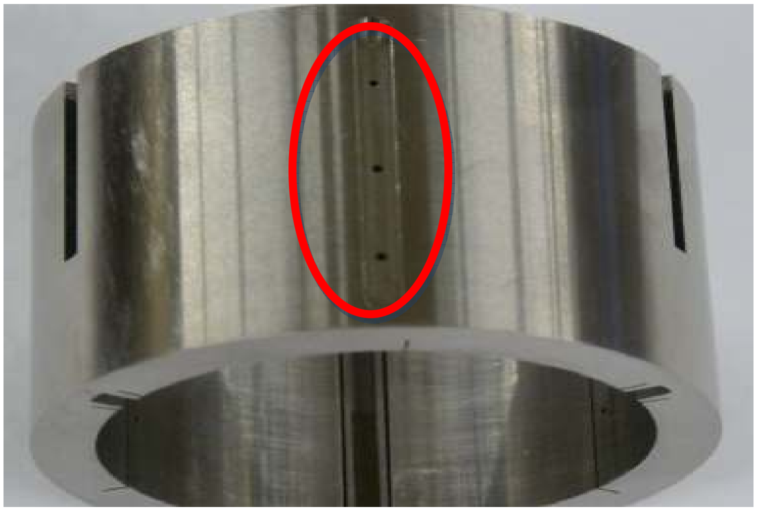

Figure 7.1 Holes on the bearing sleeve for radial air injection

Figure 7.2 Holes on the bearing sleeve for radial air injection

APPENDIX A

DRAWINGS OF ELECTRIC FURNACE

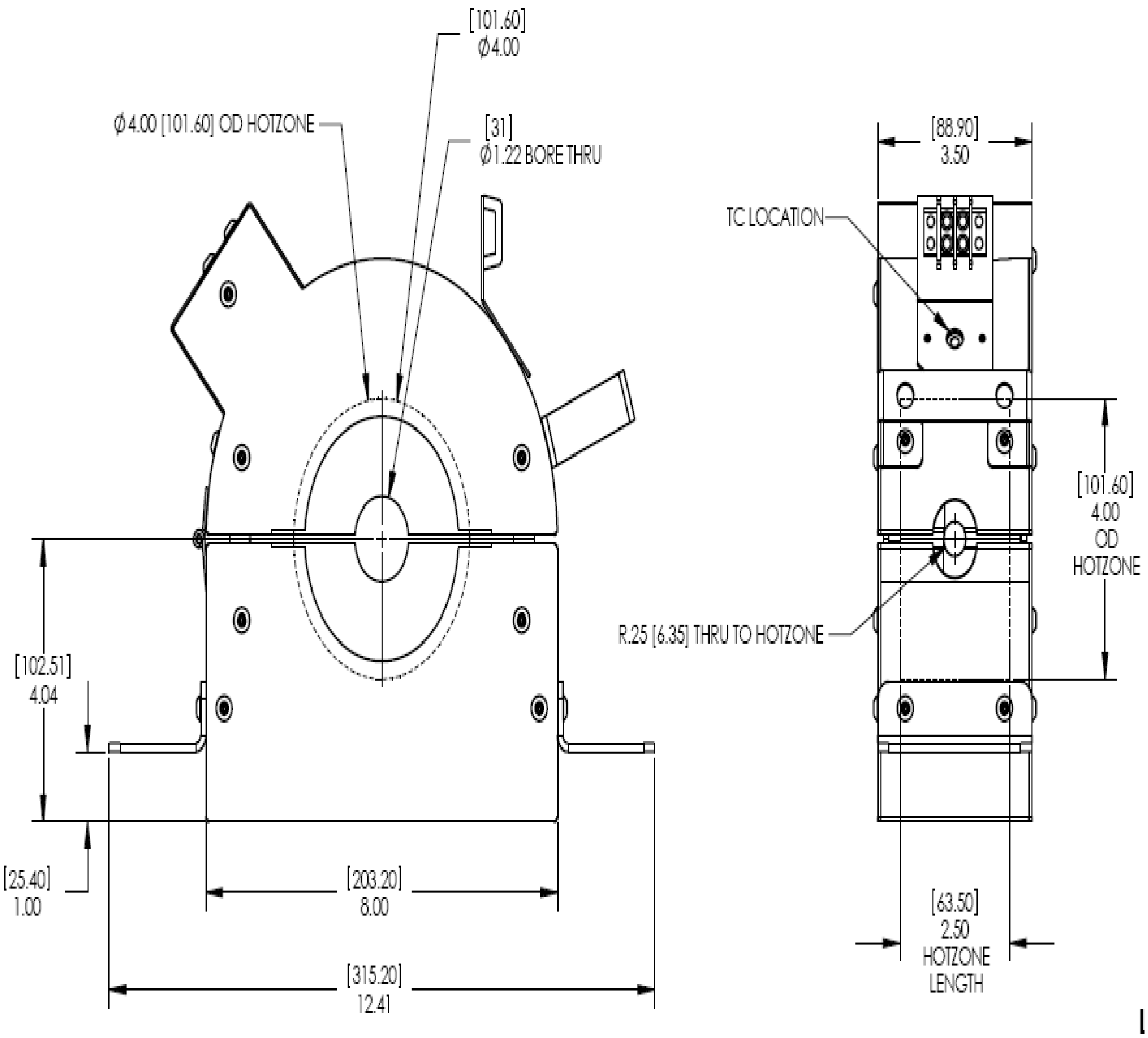

Figure A.1 Front and Side view of the custom designed furnace

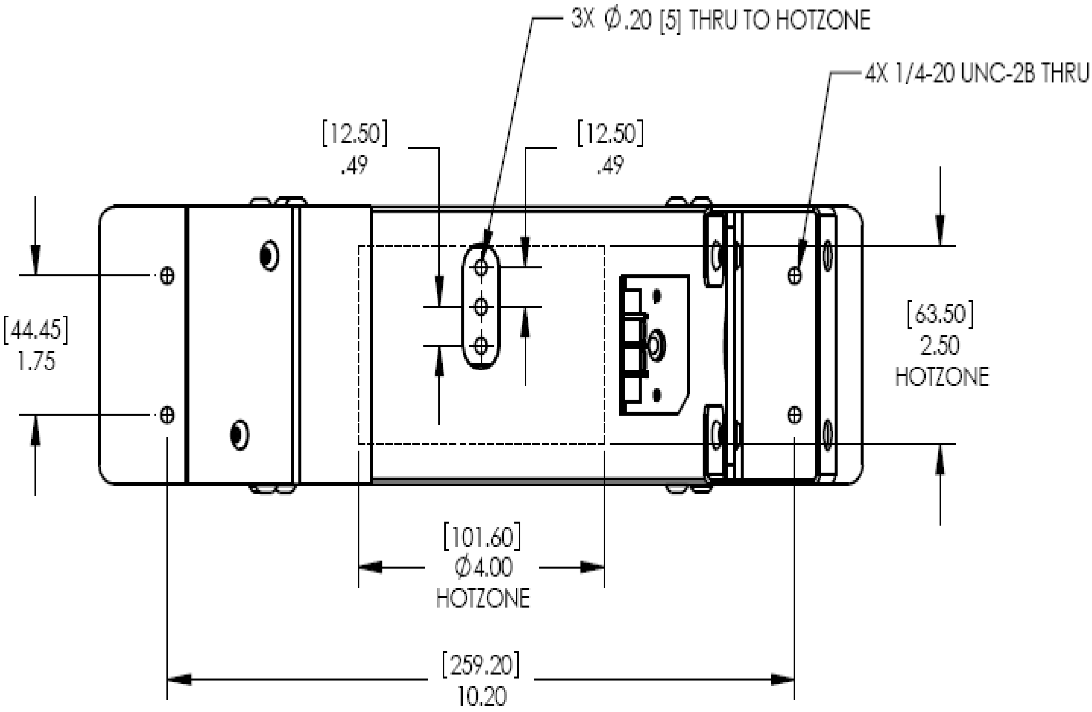

Figure A.2 Top View of the custom designed furnace

APPENDIX B

TEST RIG PICTURES

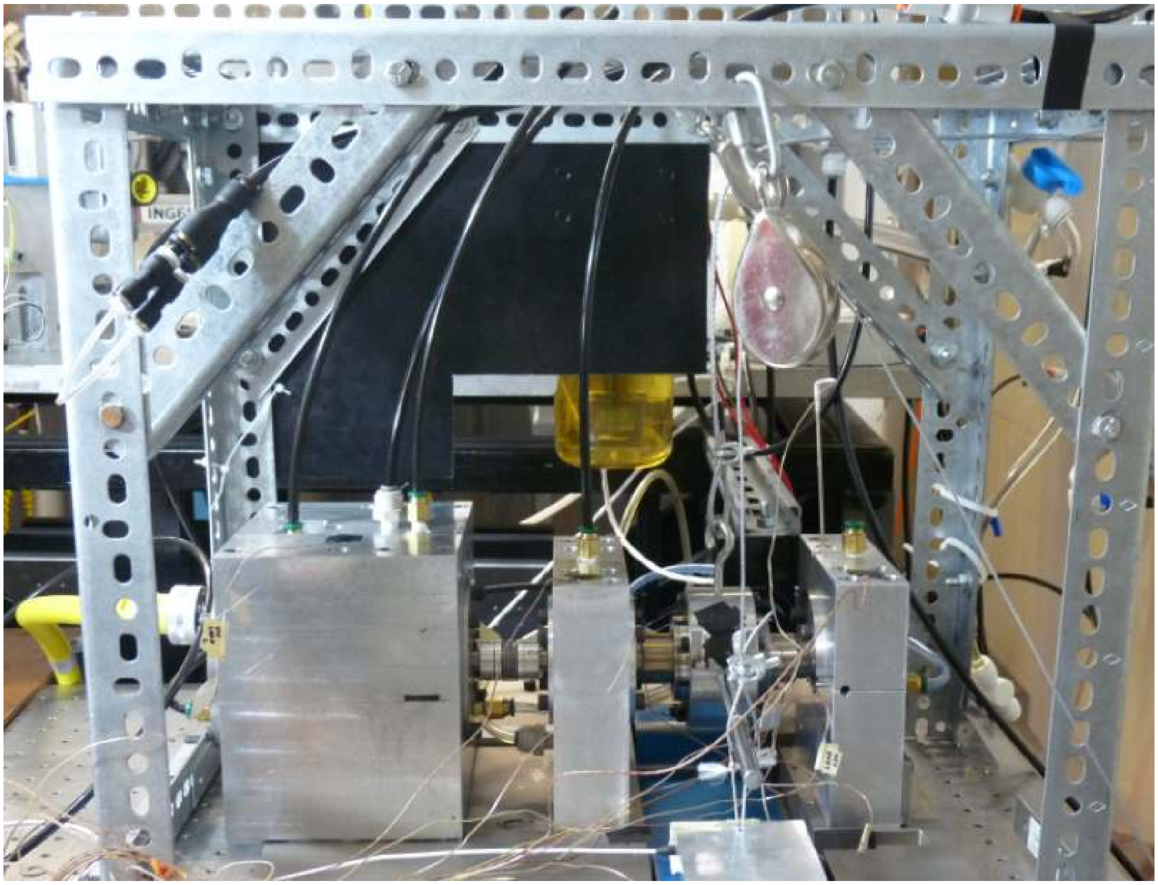

Figure B.1 Test rig picture - 1

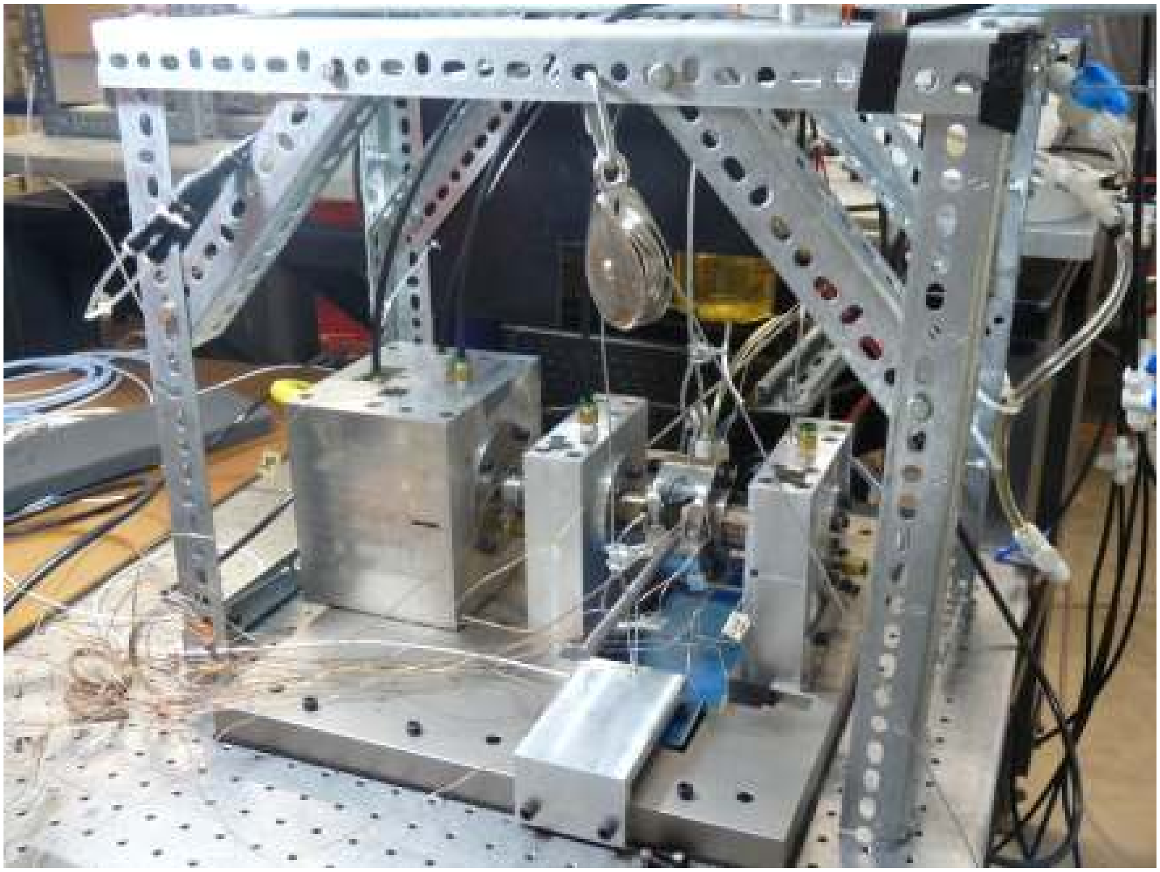

Figure B.2 Test rig picture - 2

BIBLIOGRAPHY

[1] Radil, K., and Zeszotek, M., 2004, "An Experimental Investigation into the Temperature Profile of a Compliant Foil Air Bearing," STLE Tribology Transactions**, 47**(4), pp. 470-479.

[2] Zhu, X., and San Andrés, L., 2004, "Rotordynamic Performance of Flexure Pivot Hydrostatic Gas Bearings for Oil-Free Turbomachinery," ASME Turbo Expo 2004, Vienna, Austria, ASME Paper No. GT2004-53621.

[3] DellaCorte, C., 1998, "A New Foil Air Bearing Test Rig for use to 700C and 70,000 RPM," STLE Tribology Transactions**, 41**(3), pp. 335-340.

[4] Salei, M., Swanson, E., and Heshmat, H., 2001, "Thermal Features of Compliant Foil Bearings – Theory and Experiments," ASME Journal of Tribology**, 123**(3), pp. 566-571.

[5] Radil, K., Howard, S., and Dykas, B., 2002, "The Role of Radial Clearance on the Performance of Foil Air Bearings," STLE Tribology Transaction**, 45**(4), pp. 485-490.

[6] DellaCorte, C., and Valco, M. J., 2000, "Load Capacity Estimation of Foil Air Journal Bearings for Oil-Free Turbo-Machinery Applications," STLE Tribology Transaction**, 43**(4), pp. 795-801.

[7] Peng, Z. C., and Khonsari, M., 2006, "A Thermohydrodynamic Analysis of Foil Journal Bearings," ASME Journal of Tribology**, 128**(3), pp. 534-541.

[8] Kim, D., and Park, S., 2009, "Hydrostatic Air Foil Bearings: Analytical and Experimental Investigations," Elsevier Tribology International**, 42**(3), pp. 413-425.

[9] Radil, K., DellaCorte, C., and Zeszotek, M., 2007, "Thermal Management Techniques for Oil-Free Turbomachinery Systems," STLE Tribology Transactions**, 63**(10), pp. 319-327.

[10] Kim, T. H., and San Andrés, L., 2010, "Thermohydrodynamic Model Predictions and Performance Measurements of Bump-Type Foil Bearing for Oil-Free Turboshaft Engines in Rotorcraft Propulsion Systems," ASME Journal of Tribology**, 132**, pp. 011701.

[11] Lee, D., and Kim, D., 2010, "Thermo-Hydrodynamic Analyses of Bump Air Foil Bearings with Detailed Thermal Model of Foil Structures and Rotor," ASME Journal of Tribology**, 132**(2), pp. 021704 (12 pages).

[12] Sim, K., and Kim, D., 2007, "Design of Flexure Pivot Tilting Pads Gas Bearings for High-Speed Oil-Free Microturbomachinery," ASME Journal of Tribology**, 129**, pp. 112-119.

[13] Kim, D., Lee, D., Kim, Y. C., and Ahn, K. Y., 2010, "Comparison of Thermo-Hydrodynamic Characteristics of Airfoil Bearings with Different Top Foil Geometries," Proceedings of the 8th IFToMM International Conference on Rotordynamics, Seoul, Korea, September 12-15.

[14] Kim, D., 2007, "Parametric Studies on Static and Dynamic Performance of Air Foil Bearings with Different Top Foil Geometries and Bump Stiffness Distributions," ASME Journal of Tribology**, 129**(2), pp. 354-364.

[15] Kim, D., and Lee, D., 2010, "Design of Three-Pad Hybrid Air Foil Bearing and Experimental Investigation on Static Performance at Zero Running Speed," Journal of Engineering for Gas Turbine and Power, in Print.

BIOGRAPHICAL INFORMATION

Ramesh Pandeshwara Sadashiva obtained his Bachelor’s degree in Mechanical Engineering from Visvesvaraya Technological University, India. He is currently pursuing his Master of Science degree in Mechanical Engineering at The University of Texas at Arlington, USA. He joined Microturbomachinery and Energy system laboratory under Dr. Daejong Kim in fall 2008. His research interest includes gas bearings technology, Lubrication theory of bearings and Rotor dynamics.